1

Multiwavelength Observations of Accretion in Low-Mass X-ray Binary Systems

Robert I. Hynes[a]

Abstract

This work is intended to provide an introduction to multiwavelength observations of low-mass X-ray binaries and the techniques used to analyze and interpret their data. The focus will primarily be on ultraviolet, optical, and infrared observations and their connections to other wavelengths. The topics covered include: outbursts of soft X-ray transients, accretion disk spectral energy distributions, orbital lightcurves in luminous and quiescent states, super-orbital and sub-orbital variability, line spectra, system parameter determinations, and echo-mapping and other rapid correlated variability.

1.1 Introduction

The first X-ray binary to be observed and identified as such was Scorpius X-1 (Giacconi et al., 1962), although several other systems were known as optical stars or novae before this. Within a few years, optical and radio counterparts to Sco X-1 were discovered (Sandage et al., 1966; Andrew and Purton, 1968), and the topic has remained multiwavelength in nature since then.

This work is intended to provide an introduction to some of the observational characteristics of X-ray binaries suitable for a graduate student or an advanced undergraduate. My aim was to produce a primer for someone relatively new to the field rather than a comprehensive review. Where appropriate I will also discuss techniques for analysis and inter-

[a] Louisiana State University, Department of Physics and Astronomy, 202 Nicholson Hall, Tower Drive, Baton Rouge, LA 70803, USA

pretation of the data. The focus is almost exclusively on low-mass X-ray binaries, in which the accretion disk is most accessible to multiwavelength observations, and is predominantly biased towards ultraviolet, optical, and infrared observations, and their relation to observations at other wavelengths. For a textbook treatment of accretion astrophysics in general, the reader is referred to Frank et al. (2002) and for more comprehensive reviews of X-ray binaries to Lewin et al. (1995) and Lewin and van der Klis (2006).

We begin in Section 1.2 by presenting an overview of the main classes of X-ray binaries and their accretion geometries, and in Section 1.3 describe observations of transient systems. We will then address different types of observations in turn. In Section 1.4 we examine expected and observed spectral energy distributions, in Section 1.5 we move on to consider orbital lightcurves, together with variability on super-orbital and sub-orbital (but still relatively long) timescales. Section 1.6 then examines spectroscopic observations, with a focus on determination of binary system parameters, and finally Section 1.7 looks at shorter timescale variations and in particular correlations between the X-ray and UV/optical/IR behavior. For reference, we include a glossary of notable objects in Section 1.10 and of acronyms used in Section 1.11.

1.2 Classification and Geometry of X-ray binaries

The family of X-ray binaries is diverse. A single hierarchical classification system is insufficient and depending on the question to be asked one may desire to classify objects by the nature of their donor star and mode of accretion, by the nature of the compact object, or by whether their X-ray activity is persistent or transient. Additionally, a subset of these objects produce relativistic jets and are classified as microquasars

The most common division made is into high-mass and low-mass X-ray binaries: HMXBs and LMXBs. This is based crudely on the mass of the donor star, with HMXBs typically having O or B type donors of mass over $10\,\mathrm{M}_\odot$ and LMXBs having late-type G–M donors with masses below $\sim 1.5\,\mathrm{M}_\odot$. Classification of those systems with A or F donors has been vaguer, but these objects such as Her X-1 and GRO J1655–40 have often been grouped as intermediate-mass X-ray binaries, or IMXBs. The donor mass also provides the primary division in accretion mode, with LMXBs and IMXBs mostly accreting by Roche lobe overflow (see Fig. 1.1) and HMXBs by either lobe overflow, capture of wind from the donor star,

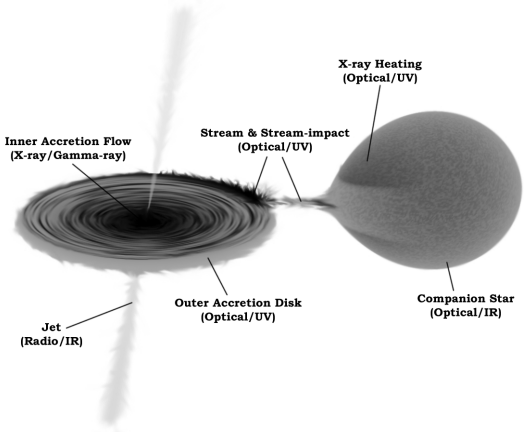

Figure 1.1 Geometry of a Roche lobe overflow low-mass X-ray binary. The color scale is inverted with the brightest areas appearing darkest.

or interaction of the compact object with a circumstellar disk. A small group of LMXBs with low-mass red giant donors do accrete from the donor wind. These are referred to as symbiotic X-ray binaries (Corbet et al., 2008). Among the LMXBs, those with exceptionally short periods and hydrogen deficient donors are often broken out into the sub-class of ultracompact X-ray binaries (UCXBs).

Another distinction can be made between systems containing black holes and those containing neutron stars. For many purposes, this is more important than the donor nature or accretion mode, and we observe many similarities in X-ray behavior between black holes in LMXBs and HMXBs.

Observationally, an important difference is found between persistent and transient sources. As time has passed this distinction has blurred, and while there remain simple classical transients like A 0620–00 which undergo dramatic outbursts every few decades, other systems seem to turn on into a semi-persistent state, or execute a whole series of outbursts in succession after emerging from quiescence. As our baseline extends, this kind of quasi-persistent, or quasi-recurrent behavior with distinct on and off periods may become a more common characteristic.

Finally, we should mention the category of microquasars. This term has had varying usage, but in the context of X-ray binaries it usually refers to those sources showing resolved, expanding, relativistic jets such as GRS 1915+105 (Mirabel and Rodríguez, 1994). Its usage has varied

from this fairly exclusive definition, to including all jet sources, to potentially all black hole binaries, and possibly also some neutron star sources.

1.3 Transient X-ray binaries

1.3.1 Classical Soft X-ray Transients

The outburst of the transient LMXB A 0620–00 in 1975 (Kuulkers 1998 and references therein) opened up what was to become a major area of X-ray binary research. It was not the first transient X-ray source found, but was the first to be studied in great detail, and the brightest yet seen.

Among the many reasons for the modern importance of transient systems, their large dynamic range is invaluable. In a single object, on a practical timescale of months to a few years we can watch the evolution of the system through the full range of accretion states and follow causal sequences between them. This is impossible with persistent X-ray binaries and active galactic nuclei (AGN), both of which individually sample a smaller range of parameter space leaving us to attempt to build a complete picture from snapshots of different objects. Another important characteristic of transient LMXBs is that in quiescence their light usually becomes dominated by their companion star. Radial velocity studies then allow measurement of system parameters, and particularly the compact object mass. This is how we know of the most compelling examples of stellar mass black holes, and that the majority of known transient LMXBs are black hole systems. We will consider system parameter determinations in more detail in Section 1.6.3.

These transient LMXBs are often referred to as Soft X-ray Transients (SXTs) based on the ultrasoft spectra that are sometimes seen in outburst or Black Hole X-ray Transients (BHXRTs) due to their high incidence of black holes. Among them is a subset which shows a relatively orderly behavior with common features repeated between several objects. The outbursts of these objects are known as FREDs – Fast Rise Exponential Decay outbursts. FRED outbursts are often considered to be typical of SXTs, but in fact there are many exceptions. In the sample of outburst lightcurves compiled by Chen et al. (1997), there are both FREDs and irregular outbursts. Since then, we have seen a preponderance of irregular outbursts and the orderly FRED behavior now seems the exception rather than the rule. Nonetheless, such a repeating pat-

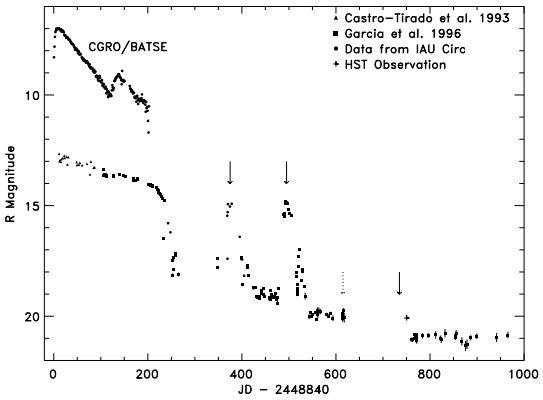

Figure 1.2 Outburst lightcurves of GRO J0422+32 adapted from Hynes and Haswell (1999). This shows many of the features of a canonical SXT outburst; a fast rise, exponential decay, and mini-outbursts. Note that the secondary maximum seen prominently in the CGRO/BATSE lightcurve is not the one discussed in the text. The one discussed occurs earlier and is much less prominent in this object.

tern is a natural place to begin in trying to understand their behavior and has provided the benchmark for numerical simulations of outburst lightcurves (e.g. Cannizzo et al. 1995; Dubus et al. 2001; Truss et al. 2002).

We show the hard X-ray (CGRO/BATSE) and optical lightcurves of GRO J0422+32 in Fig. 1.2 as an example of a FRED lightcurve showing most of the common characteristics. The outburst exhibits a very fast rise followed by a slow exponential decay for about 200 days. During the decay there are several secondary maxima. At the end of the exponential decay comes a rapid drop-off. After this the outburst was below the CGRO/BATSE threshold, but continued evolution could be seen in the optical, with a continued decline interrupted by at least two mini-outbursts.

The accepted framework for understanding SXT outbursts is believed to be the disk instability model (DIM, Lasota 2001) originally developed to explain outbursts of dwarf novae (DNe). The latter usually have a much shorter recurrence time and non-exponential decays. The exponential decay in SXTs has been explained by King and Ritter (1998) as a consequence of irradiation maintaining the whole disk in the hot, high viscosity state of the DIM. The accretion rate is proportional to the

active disk mass, and so if the luminosity traces the accretion rate, then the exponential decay in luminosity reflects the decay of the disk mass. For short-period systems where it is possible to maintain the whole disk in a high state in this way, it is possible to accrete a large fraction of the disk mass during an outburst. Consequently, the recurrence time is longer than in DNe, where only a small fraction of the disk mass is accreted in a single outburst.

Several explanations have been advanced for the secondary maxima, and different features at different points in the decay may have different explanations. In the earliest explanations, the turn-on of X-rays during the outburst irradiated the companion star and stimulated a burst of enhanced mass transfer into the disk. When this material reached the compact object, the X-ray flux was further increased (Chen et al., 1993; Augusteijn et al., 1993). King and Ritter (1998) instead proposed that initially there is an outer region of the disk that begins the outburst in the cool low viscosity state of the DIM. Irradiation at the onset of the outburst then raises this to the high state, and again, its effect on the X-ray lightcurve is delayed by one viscous time. Finally Truss et al. (2002) modified this mechanism by instead invoking the growth of tidal instabilities as a mechanism to stimulate accretion from the outermost part of the disk.

The explanation for mini-outbursts remains less conclusive. This phenomenon has been less commonly observed in SXTs, as it happens later when the source has passed below the threshold of all-sky monitors and so is typically mostly covered by sparser optical coverage. These mini-outbursts are also characterized by a higher ratio of optical to X-ray flux. The phenomenon closely resembles the 'echo-outbursts' seen in some cataclysmic variables (CVs) where on occasion as many as six roughly uniformly spaced mini-outbursts have been seen (Patterson et al., 1998). In attempting to explain mini-outbursts, Hameury et al. (2000) again invoked irradiation, Osaki et al. (2001) attributed them to failed viscosity decay attempts at the end of the outburst, while Hellier (2001) associates them with tidal effects.

Once again, it should be emphasized that only a minority of SXT outbursts follow the classic FRED form (and indeed that not all SXT outbursts even exhibit the defining ultrasoft state; Brocksopp et al. 2004). In many cases the irregular outbursts are associated with longer period systems where it may not be possible to raise all of the accretion disk into the hot state resulting in interactions between the hot inner disk and the permanently cold outer region. However, some short period systems

such as XTE J1118+480 also exhibit irregular (and recurrent) outburst activity.

1.3.2 Recurrent transients and semi-persistent systems

It is likely all transient systems are recurrent, of course, but some recur on shorter timescales than others. The best defined of these are systems where outbursts occur once per orbital period, usually near closest approach (periastron). The Be star plus neutron star HMXBs are the most common example of this type, but Cir X-1 is another eccentric transient system.

Some transient LMXB sources emerge from quiescence to undergo multiple recurrent outbursts like GRO J1655–40, or turn on without subsequently returning to quiescence like GRS 1915+105. GX 339–4 is sometimes thought of as a rare persistent black hole but is actually more like a very active recurrent transient, and given a longer baseline may turn out to have been discovered in the midst of a short-lived series of outbursts.

Among neutron stars, we see several that exhibit a similar kind of semi-persistent behavior. 4U 2129+47 was identified as a 5.2 hr LMXB by Thorstensen et al. (1979) only to fade to quiescence in 1983 (Pietsch et al., 1983). EXO 0748–676 went into outburst in 1985 (Parmar et al., 1985), remained as an apparently persistent source for 24 years, before finally returning to quiescence in 2008.

This behavior among neutron stars provides a unique tool to probe the properties of the neutron star. During an outburst, the crust is heated by accretion and is no longer in thermal equilibrium with the core. The cooling curve of the neutron star after outburst then depends sensitively on the thermal conductivity of the crust, so these observations can be used to test models for the structure and composition of neutron star crust and the crust-core interface (Brown and Cumming, 2009).

1.4 Spectral Energy Distributions

1.4.1 Overview

X-ray binaries are multiwavelength objects with detectable emission from radio to gamma-rays and at all wavelengths in between. The spectral energy distribution (SED) measures the relative energy contributed

in different bands, and crudely characterizes the shape of the spectra. The SED can inform us of the different components emitting, in particular the disk, and the structure of those components. Without additional spatial constraints, such as might be provided by eclipse-mapping, we do not obtain any information about the spatial arrangement of emitting regions, so there may be degenerate models. In the simplest case of black body emission from an accretion disk the information gained is really a measure of how much emitting area is present at each temperature. With the common assumptions that the disk is axisymmetric and that the temperature increases monotonically inwards, however, we can translate this information into the temperature as a function of radius. In practice, it is more common to make these assumptions and fit simple derived models to the SED, and so we will focus on the basis of these models.

At this point there are many different representations of the SED in use and it is unlikely that a common standard will be adopted. It is worthwhile to be familiar with the different conventions and to be able to mentally transform between them. In order to show the order of magnitude range of values typically present, almost all authors use logarithmic axes for both the energy/wavelength axis and for flux. In the X-ray binary community it is common to use an energy-like x-axis, either based on photon frequency (ν) or energy (E). The y-axis is either the flux per unit frequency, F_ν (or equivalently per unit energy, F_E), or this multiplied by the photon energy. Examples of SEDs in the $\nu - F_\nu$ representation are shown in Figs. 1.3 and 1.4. A straight F_ν representation makes it easier to estimate the spectral index, α, of a power law expressed as $F_\nu \propto \nu^\alpha$. In particular, this representation is well suited to the typically flat ($F_\nu \simeq$ constant) radio spectra often seen and associated with jets. On the other hand, in a plot of $\log \nu F_\nu$ vs. $\log \nu$, the height in νF_ν is a direct measure of the amount of energy emerging per logarithmic frequency interval at that frequency, hence the peak of an SED in νF_ν is the energetically most important component. A $\nu - \nu F_\nu$ SED is also shown in Fig. 1.3. The most common SED forms encountered in X-ray binary work are then $\nu - F_\nu$, $\nu - \nu F_\nu$, $E - F_E$, and $E - EF_E$, with the latter two most common in dealing with X-ray and gamma-ray data. Wavelength based forms are sometimes used, $\lambda - F_\lambda$ or $\lambda - \lambda F_\lambda$. To mentally transform between them, it is helpful to remember that a power-law of $F_\nu \propto \nu^\alpha$ becomes $F_\lambda \propto \lambda^{2-\alpha}$ in this representation. The final variation on these representations is unique to X-ray and gamma-ray astronomy where the spectrum is sometimes described in an $N_E - E$

representation where N_E is the number of photons per unit energy interval. Power-law spectra are then specified by the photon index, Γ, where $N_E \propto E^{-\Gamma}$. Note the negative sign in the definition. The photon index is related to the $F_\nu - \nu$ spectral index by $\Gamma = 1 - \alpha$.

1.4.2 The Black Body Disk Model

The spectral model that has most commonly been fitted to optical and UV SEDs of X-ray binaries is a black body based model (Lynden-Bell, 1969; Shakura and Sunyaev, 1973; Frank et al., 2002). The disk is assumed to be axisymmetric, with temperature increasing inwards. Having defined the functional form of $T(R)$, the SED is evaluated by summing emission from each concentric annulus. Simple limiting cases can be derived analytically, but with realistic assumptions (for example that both viscous and irradiative heating are present), a numerical integration is more useful.

The problem can be defined for a power-law temperature distribution:

$$T(R) = T_0 \left(\frac{R}{R_0}\right)^{-n} \tag{1.1}$$

In the commonly discussed steady-state disk, $n = 3/4$ (Shakura and Sunyaev, 1973). We assume a local black body spectrum, B_ν:

$$B_\nu(R) = \frac{2h\nu^3}{c^2\left(e^{h\nu/kT(R)} - 1\right)} \tag{1.2}$$

and write the integrated SED of the disk as:

$$F_\nu = \frac{2\pi\cos i}{D^2}\int_{R_{\rm in}}^{R_{\rm out}} B_\nu(R) R dR \tag{1.3}$$

where D is the source distance and i is the binary inclination. This leads to the general solution:

$$F_\nu = \nu^{3-2/n}\frac{4\pi h^{1-2/n}\cos i k^{2/n} T_0^{2/n} R_0^2}{nc^2D^2}\int_{x_{\rm in}}^{x_{\rm out}} \frac{x^{2/n-1}dx}{e^x - 1} \tag{1.4}$$

where the substitution $x = h\nu/kT$ has been made. In the limiting case of an unbounded disk extending from zero radius to infinity, the integral is just a numerical value and the frequency dependence extracted is $F_\nu \propto \nu^{3-2/n}$. For the Shakura-Sunyaev disk, $n = 3/4$, we obtain the well known result $F_\nu \propto \nu^{1/3}$. If the disk is irradiatively heated then the simplest assumption is that the irradiating flux drops off as the inverse

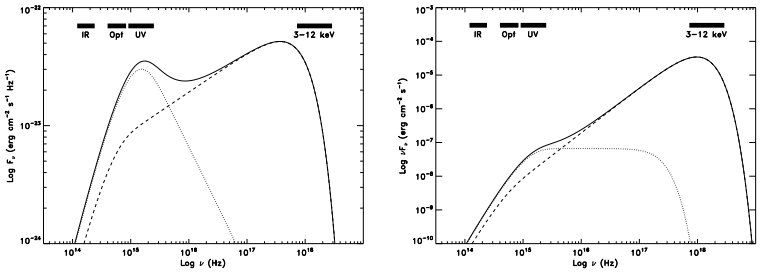

Figure 1.3 Black body SED for cases with viscous heating (dotted), irradiative heating (dashed) and a combination of the two (solid). The left hand panel shows the $\nu - F_\nu$ representation, the right hand panel shows the same models in the $\nu - \nu F_{nu}$ representation.

square of the radius leading to $T^4 \propto R^{-2}$ and $T \propto R^{-0.5}$. The resulting SED should then exhibit $F_\nu \propto \nu^{-1}$, a red spectrum actually decreasing into the UV.

In practice, since the irradiation temperature $T_{\rm irr} \propto R^{-0.5}$ drops off more slowly as a function of radius than the temperature due to viscous heating, $T_{\rm visc} \propto R^{-3/4}$, we expect the inner disk to be dominated by viscous heating and the outer by irradiation, leading to a spectrum that turns over between the two limits at some intermediate frequency (Fig. 1.3). Furthermore, the disk does not extend from zero radius to infinity, and both inner and outer bounds are important in defining the spectrum. The inner radius influences the X-ray spectrum and the outer radius the UV and optical. Modeling of real X-ray data is more complex than described here. Firstly, the temperature distribution of the inner disk is modified by the boundary condition applied at the inner edge of the disk. Secondly, Comptonization changes the X-ray spectrum substantially (see Chapter by Done).

1.4.3 Multiwavelength Observations of Black Holes in Outburst

The first really high quality data set with which to test the picture described above came from IUE and HST observations of the black hole system X-ray Nova Muscae 1991 (Cheng et al., 1992). Multiple epochs of data as the source faded revealed an approximately $F_\nu \propto \nu^{1/3}$ spectrum consistent with a viscously heated accretion disk. Taken at face value, however, this interpretation requires extremely high accretion rates com-

parable to or in excess of the Eddington limit (the accretion rate at which radiation pressure balances gravity and can suppress further accretion).

Improvements in HST capabilities, and target of opportunity strategies led to a much richer dataset on XTE J1859+226 (Fig. 1.4; Hynes et al. 2002), both in wavelength and temporal coverage. Early observations showed a smooth spectrum with a broad hump in the UV well fitted by black body disks with a relatively flat temperature distribution consistent with an irradiated disk. Later in the outburst, the far-UV spectrum transformed from a UV-soft form, where f_ν declined with ν to a rising UV-hard form, consistent with expectations of a purely viscously heated disk and similar to that seen in X-ray Nova Mus 1991.

Other black hole transients have had less complete coverage but show similar characteristics. A 0620–00 showed a UV-hard SED resembling X-ray Nova Mus 1991 or XTE J1859+226 at late times, while GRO J0422+32 was UV-soft like XTE J1859+226 at early times (Hynes 2005 and references therein).

It should be emphasized that the primary diagnostic between the UV-hard and UV-soft states (and by inference R^{-3} and R^{-2} heating) is the turnover or its absence in the UV, and the slope of the far-UV spectrum. Hynes (2005) showed SEDs of these systems and others based only on the optical portion of the SED, and no such discrimination was possible. To obtain a reliable SED requires not only good coverage in the satellite UV (for which HST is ideal, but Swift/UVOT lacks far-UV capability), but also a good understanding of the effect of interstellar reddening on the SED. For a discussion of the latter, see Fitzpatrick (1999) and references therein.

1.4.4 Irradiation of Disks

The amount of irradiation of the accretion disk that is actually expected has been examined by Dubus et al. (1999) and expressed somewhat differently by Dubus et al. (2001). They express the local irradiation temperature for a disk element at radius R as:

$$\sigma T_{\rm Irr}^4 = \mathcal{C}\frac{L_{\rm X}}{4\pi R^2} \tag{1.5}$$

where σ is the Stefan-Boltzmann constant, $L_{\rm X}$ is the irradiating (X-ray) luminosity, and $\mathcal{C}$ is a dimensionless measure of the efficiency of irradiation. $\mathcal{C}$ parametrizes our ignorance of the illumination geometry and the (energy-dependent) albedo of the disk element. Empirically, Dubus

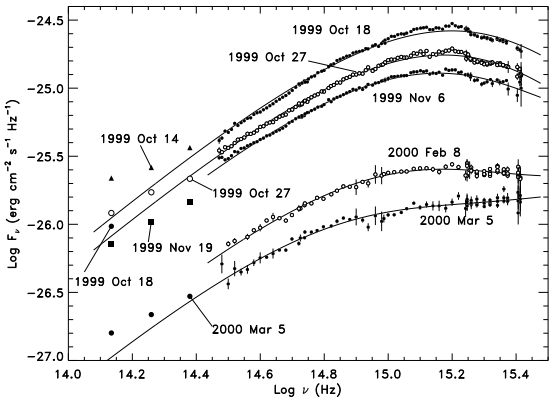

Figure 1.4 Observed SEDs of XTE J1859+226 from Hynes et al. (2002). Different symbols are used to differentiate different observation dates.

et al. (2001) find that a value of $\mathcal{C} \simeq 5 \times 10^{-3}$ is consistent with observations.

One difficulty with this simple picture that has been appreciated for some time is that models of disk structure usually predict a disk profile that is convex as a function of radius (Dubus et al. 1999 and references therein). Such a disk should be self-shielding and the inner portion should be unable to irradiate the outer regions, in spite of considerable evidence (such as echo-mapping; Section 1.7) that accretion disks do experience irradiation. Dubus et al. (1999) suggest that either X-rays are scattered by material out of the plane or that warping of the accretion disk (see Section 1.5.5) can expose portions of the outer disk to irradiation. In this case, $\mathcal{C}$ also parametrizes our ignorance about how irradiation of the disk is mediated. The caveat here is that for many accretion geometries, $\mathcal{C}$ itself becomes a function of radius.

One example where the radial dependence of irradiation can be significantly modified is important to discuss, and to highlight how an inferred temperature distribution may not be sufficient to constrain the underlying astrophysics. This is the case of irradiation by a 'lamp post' above the disk, for example flares in a vertically extended corona, or back-irradiation from a jet. This case is well known in the AGN and young star communities where it is sometimes considered the normal irradiation geometry. It is illustrated in Fig. 1.5. In this case, the intensity of irradiating flux decreases according to the inverse square law as consid-

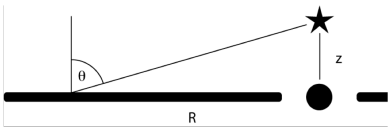

Figure 1.5 Irradiation geometry appropriate for a 'lamp post' above the accretion disk.

ered above, but in addition the angle of incidence becomes steeper at larger radii resulting in spreading the irradiation over a larger area. This introduces another factor proportional to $\cos\theta \simeq z/R$ for $z \ll R$ (where z is the height of the irradiating source above the disk). The additional $1/R$ dependence results in heating varying as R^{-3} just as for the viscously heated steady state accretion disk. It is therefore possible that the UV-hard spectra discussed above could also result from irradiation, and this may avoid the difficulty noted, for example in the case of X-ray Nova Muscae 1991, where purely viscous heating would require accretion at or above the Eddington limit.

1.4.5 Evidence for Jets in Spectral Energy Distributions

Not all emission in the spectral energy distributions of LMXBs originates in the disk. There is now very persuasive evidence in a number of black hole LMXBs for IR synchrotron emission from a jet. This is seen as either a flat IR spectrum extending to lower frequencies than possible for the disk (XTE J1118+48; Hynes et al. 2000) or even a two component spectrum with a red IR component from the jet and a blue disk component (GX 339–4; Corbel and Fender 2002). In both cases the IR flux is comparable to that seen in the radio as expected from extrapolation of the characteristic flat spectrum of a compact radio jet (Blandford and Konigl, 1979). More recently a similar SED has also been seen in the neutron star LMXB 4U 0614+091 (Fig. 1.6; Migliari et al. 2006, 2009). The second observation was based on quasi-simultaneous observations of a persistent source and so is a robust measure of the SED.

Another signature expected for synchrotron emission from a jet would be polarization. To date no large IR polarizations have been found, although Shahbaz et al. (2008a) saw polarizations in Sco X-1 and Cyg X-2 of a few percent which increased with wavelength as would be expected from the increasing fractional contribution of a jet at longer wavelengths, and which were not consistent with expected interstellar polarization.

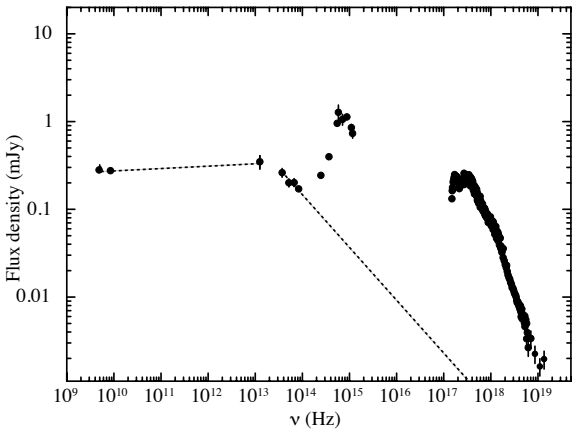

Figure 1.6 SED of 4U 0614+091 adapted from Migliari et al. (2009).

1.4.6 Quiescent SEDs

Observations of quiescent LMXBs also reveal emission across most of the observable range, although radio detections are extremely challenging and those at gamma-ray energies have been impossible so far. A major complication in obtaining SEDs of the accretion emission in quiescent LMXBs is that the companion star can completely dominate the optical and IR range of the spectrum. Unfortunately, the brightest quiescent system, V404 Cyg, also exhibits almost complete dominance of the UV to near-IR SED by the companion (Hynes et al., 2009b).

The accretion flow is clearly detected at X-ray energies in many systems, and appears to be characterized by a soft power-law of photon index $\Gamma \sim 2$, corresponding to $F_\nu \propto \nu^{-1}$ (e.g. Kong et al. 2002). This almost certainly originates from the inner region of the accretion flow which is believed to form a hot, evaporated, advective flow. Spectral models of such flows variously attribute the X-ray emission to either bremmstrahlung or Comptonization, but there remain many uncertainties in these models and there is no uniquely accepted solution (Narayan et al., 1996, 1997; Esin et al., 1997; Quataert and Narayan, 1999). X-ray emission lines could provide a valuable discriminant (Narayan and Raymond, 1999), but the most sensitive observations of a quiescent SXT, XMM-Newton observations of V404 Cyg, yielded only upper limits on the iron Kα emission line that is expected to be strongest (Bradley et al., 2007).

A UV excess is sometimes detectable (McClintock et al. 1995; McClintock and Remillard 2000; McClintock et al. 2003; Hynes et al. in preparation). The spectral shape can be characterized as a hot quasi-blackbody of temperature $\sim 10,000\,\mathrm{K}$. Our best explanation for this component currently is that it either originates from the accretion stream-impact point, or from a relatively hot region of the disk (hot enough that it should be locally in the high state of the DIM).

A mid-IR excess is also seen (Muno and Mauerhan, 2006) but the origin remains debated. In some sources such as V404 Cyg, the excess is rather subtle, but in others like A 0620–00 and XTE J1118+480 it is very pronounced and clearly real. The favored explanation of Muno and Mauerhan (2006) for most sources was that it originates in a *circumbinary* accretion disk comprising material lost during outbursts or even the original supernova that formed the compact object. At longer wavelengths, radio emission appears to exhibit a flat spectrum as is often seen in more luminous states (Gallo et al., 2005). The most natural explanation for this is that a weak jet continues in quiescence. It is even possible that this dominates the quiescent energy budget with much of the accretion power carried away in the bulk kinetic energy of the jet (Fender et al., 2003). Interestingly, an extrapolation of the flat radio spectrum into the mid-IR region comes reasonably close to the IR excess flux, leading Gallo et al. (2007) to interpret the mid-IR excess as due to the jet instead of a circumbinary disk, resulting in a situation similar to the hard state systems discussed in Section 1.4.5.

1.5 Light Curves

1.5.1 Ellipsoidal Variations

The simplest form of optical lightcurve of an LMXB is that from ellipsoidal variations in quiescence where the light is often dominated by the companion star. This star is tidally distorted into a tear-drop shape. When viewed side-on at orbital phases 0.25 and 0.75, we see a large cross-sectional area and hence maximum light. When viewed end-on at phases 0.0 and 0.5 we see a smaller cross-sectional area and hence light. In essence, ellipsoidal variations then take a near-sinusoidal form with two cycles per binary orbit. An additional complication is that the surface of the companion is not uniformly bright due to gravity darkening (von Zeipel, 1924). Less flux emerges from regions of the companion with

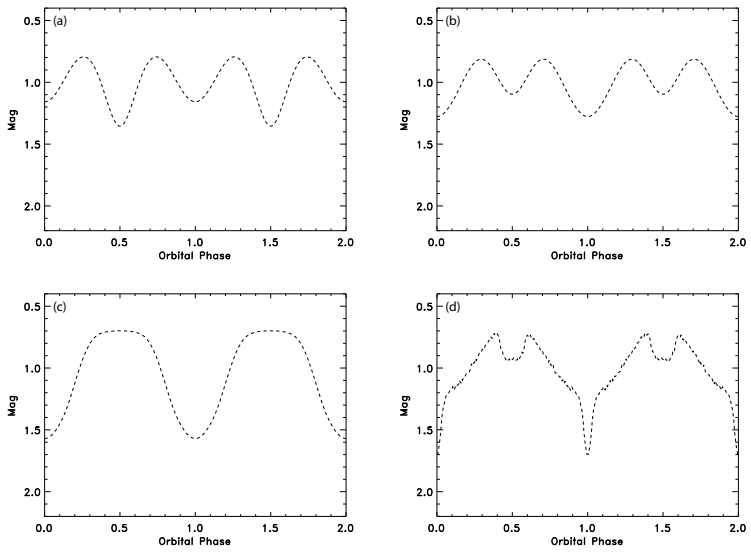

Figure 1.7 Orbital lightcurves of LMXBs. a) Pure ellipsoidal variations. b) Ellipsoidal variations plus weak irradiation of the donor. c) Strong irradiation of the donor. d) Irradiation of disk and donor with mutual eclipses. These figures were generated by the XRbinary code written by E. L. Robinson.

a lower surface gravity, and so these regions have a lower effective temperature. In the absence of significant X-ray heating of the donor star, this results in maximum surface temperature at the poles and minimum at the inner Lagrangian point facing the compact object. This breaks the symmetry between phase 0.0 and 0.5 (but not between 0.25 and 0.75). Consequently ellipsoidal variations should exhibit two equal maxima but unequal minima, with the phase 0.5 minimum being deeper. A model ellipsoidal lightcurve is shown in Fig. 1.7a.

The amplitude of ellipsoidal modulations is mostly determined by the binary inclination, with a lesser dependence on mass ratio and an even weaker dependence on stellar temperature and surface gravity (via limb darkening changes). This has made measurement of ellipsoidal modulations the technique of choice for determining inclinations of non-eclipsing quiescent LMXBs. An example is shown in Fig. 1.8.

There are several caveats to this approach. The first and most obvious is that the observed variations must actually be produced by ellipsoidal modulations. Other mechanisms for periodic variability include

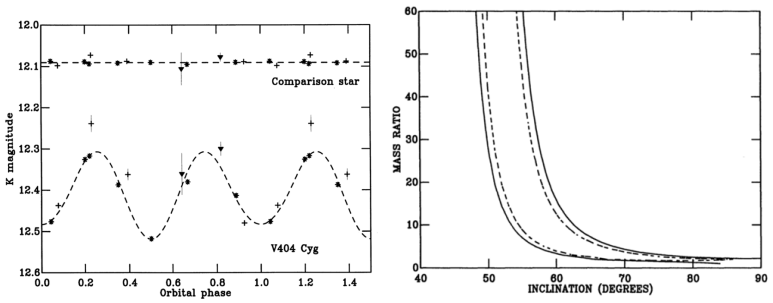

Figure 1.8 Left: IR ellipsoidal modulations in the quiescent SXT V404 Cyg with a fitted model. Right: Derived joint constraints on inclination and mass ratio. Both figures are from Shahbaz et al. (1994).

superhumps (see Section 1.5.4), variations in the visibility of the accretion stream impact point, and starspots on the companion star. There are certainly lightcurves which cannot fully be explained by ellipsoidal variations. For example many studies have now been made of A 0620–00 which find that the lightcurves clearly change in morphology from epoch to epoch, often showing asymmetric maxima (McClintock and Remillard, 1986; Haswell et al., 1993; Gelino et al., 2001; Cantrell et al., 2008). The authors have variously invoked state changes, disk asymmetries, star spots, and eclipses to explain the behavior seen. While the system is no longer believed to be at a high enough inclination to eclipse, it is likely that several of the other effects may all play a role.

Even in the absence of periodic contamination of the ellipsoidal lightcurves, the presence of non-variable disk emission will dilute the ellipsoidal variations. This will make the amplitude appear smaller leading to an underestimate of the binary inclination and ultimately an overestimate of the compact object mass. It is often argued that this contamination can be minimized by measuring IR ellipsoidal variations (e.g. Gelino et al. 2001), but an IR contamination from a cool disk might well be *expected* in quiescence (Hynes et al., 2005) and the presence of IR excesses in quiescent SXTs discussed in Section 1.4.6 reinforces this expectation. To attempt to compensate for this, one can try to measure the amount of disk light by measuring dilution of the photospheric absorption lines of the companion star; this is termed the veiling. While some measurements suggest small or undetectable IR veiling, e.g. V404 Cyg (Shahbaz et al., 1996) in other objects the IR veiling can be significant (Froning et al., 2007). In any case, we know that flickering light is present in quiescence

which can have large amplitudes (e.g. Hynes et al. 2003b), that IR flickering can be detectable (Reynolds et al., 2007), and that longer timescale changes in the overall flux level also occur (Cantrell et al., 2008). These facts suggest that even if we believe the veiling can be measured reliably, it is strictly only valid if measured simultaneously with the ellipsoidal variations, and ideally during the passive state identified by (Cantrell et al., 2008).

1.5.2 X-ray Heating Effects

As we move from quiescence into luminous or outburst states, the accretion rate onto the compact object, and hence the X-ray luminosity, increases. The first effect on the lightcurve is that the temperature of the inner face of the companion star is raised by irradiation from the increased X-ray luminosity. This offsets the gravity darkening effect and will first weaken the phase 0.5 minimum, then reverse the depths of the minima (so that phase 0.0 is the deeper minimum). With strong enough heating, such as for typical short period luminous LMXBs, the ellipsoidal effects are no longer discernible and we see a single-humped modulation with a *maximum* at phase 0.5 and a minimum at phase 0.0. This progression from pure ellipsoidal modulations to strong heating of the companion star is illustrated in Fig. 1.7a–c.

This effect is commonly observable in neutron star LMXBs allowing the orbital period to be determined from optical photometry. In many cases in the absence of X-ray eclipses or dips, this may be the first or only evidence for the orbital period. For example, in Sco X-1 the orbital period of 0.78 days was first identified in this way (Gottlieb et al., 1975).

1.5.3 Eclipses

If an LMXB has a high enough inclination, then eclipses of the accretion disk by the companion star can occur, sharpening the minimum at phase 0.0, while eclipses of the irradiated face of the companion star by the disk may introduce a secondary eclipse at phase 0.5 (Fig. 1.7d). Real lightcurves can look very much like this model, for example XTE J2123–058 (Zurita et al., 2000). At higher inclinations self-obscuration of the disk becomes an important factor and additional structure appears in the lightcurves reflecting deviations from axisymmetry of the disk. The most pronounced manifestation of this is X-ray dipping discovered in 4U 1915–05 (White and Swank, 1982) and subsequently seen in about

ten other neutron star LMXBs. X-ray dips are characterized by rather irregular dipping usually strongest around phases 0.7–1.0 likely indicating absorption by inhomogeneous material associated with the accretion stream impact point and/or material from it that overflows the disk. At even higher inclinations the central X-ray source is *permanently* obscured by the disk structure resulting in an accretion disk corona (ADC) source where only scattered X-rays are seen. The prototypical ADC source is 2A 1822–371 (Mason et al., 1980); see Bayless et al. (2010) for a recent multiwavelength study. Such sources are characterized by a much lower ratio of X-ray to optical brightness than lower inclination objects, and by broad partial X-ray eclipses rather than narrow total ones.

Eclipsing systems provide much more precise constraints on the binary inclination, and so have the potential to yield more accurate system parameters than are possible with ellipsoidal variations alone. Unfortunately, no eclipsing black hole LMXBs are known in our Galaxy so this potential benefit for black hole mass determination has yet to be fully realized. The only eclipsing black hole candidate known with confidence is the HMXB, M33 X-8 (Orosz et al., 2007). The lack of eclipsing black hole systems is unlikely to be coincidence, and reflects a selection effect leading to an absence of black hole LMXBs with inclination $i > 75°$. It is proposed that higher inclination black hole systems are ADC sources where much of the X-ray luminosity is hidden from view and so we are less likely to detect them (Narayan and McClintock, 2005). Neutron star ADC sources have been found in spite of this selection effect because they are persistently active whereas black holes are usually transient.

In CVs, eclipsing systems facilitate eclipse-mapping of the accretion disk emission structure and radial temperature dependence (see Warner's review in Chapter by Warner). This tomographic eclipse-mapping methodology developed for CVs depends on the known geometry of the companion Roche lobe occulting the disk. It has not proved directly applicable in LMXBs because of the disk self-obscuration effects together with the additional light from heating of the companion star. Instead, LMXB lightcurves have been interpreted by developing a model of the binary geometry, including irradiation of the disk and companion and possibly asymmetric structure in the accretion disk and then predicting multiwavelength lightcurves. The nature of the self-obscuration remains a matter of debate. Early models interpreted it as an elevated rim to the accretion disk. The major flaw of this explanation is that to maintain outer disk material at this elevation would require temperatures much higher than expected, so such material could not be in hydrostatic equi-

librium. Bayless et al. (2010) instead suggest that the obscuring material is a wind from the inner disk, and so is not in hydrostatic equilibrium.

Another benefit to eclipsing LMXBs is that eclipses can provide very precise timing of the orbital period, with ingress and egress times of the total eclipse of the neutron star lasting just a few seconds. The duration here reflects the scale height of the companion star atmosphere, which is larger than the neutron star size. The best studied case by far is EXO 0748–676 (Wolff et al., 2009). In this system, an ongoing eclipse monitoring program through the history of RXTE, coupled with less well sampled observations from the preceding decade, has resulted in an orbital period history with exquisite precision. Surprisingly, rather than showing a gradual period evolution, this monitoring has revealed distinct epochs of duration 5–10 years with no obvious changes in the X-ray behavior corresponding to the abrupt transitions between epochs. Wolff et al. (2009) attributed these changes to magnetic cycles in the companion star which modify its internal structure, and hence redistribute a small amount of angular momentum. In support of this interpretation, similar behavior is seen in magnetically active RS CVn systems.

1.5.4 Superhumps

It should not be assumed that all periodicities are actually orbital modulations. The tidal interaction of the companion star with the outer disk can excite eccentric modes within the disk. The most commonly encountered mode is excited when the disk grows to a radius where there is a 3:1 resonance between the local Keplerian frequency and the orbital frequency (Whitehurst and King, 1991). This is possible only in systems with relatively small mass ratios ($q = M_2/M_1 < 0.25$) as larger mass ratios result in the disk being truncated inside the 3:1 resonance radius by tidal stresses from the companion star. In even more extreme mass ratio systems, it may be possible to also excite the 2:1 resonance. Once eccentricity develops, the eccentric disk will slowly precess. When the eccentric disk reaches closest to the companion star, it experiences increased tidal stresses and hence more heating. This leads to variations in the optical and UV light from the outer disk, termed superhumps, that occur at the beat period between the orbital period and the precession period. Superhumps are commonly seen in CVs, and are discussed in more detail by Warner in Chapter by Warner, but they can occur in LMXBs too.

The most likely LMXBs to exhibit superhumps are black hole sys-

tems as these tend to have more extreme mass ratios than most neutron star LMXBs. O'Donoghue and Charles (1996) examined the cases for several black hole transients and concluded that superhumps had definitely been seen in two systems, GRO J0422+32 and X-ray Nova Muscae 1991, and had possibly also been seen in GS 2000+25. Unlike the CV case, however, where superhumps are uniquely present during outburst with the orbital period absent, in LMXBs both orbital and superhump modulations may be present, at different times or even simultaneously. The superhump period is very similar to the orbital period (to within a few percent) and discrimination between the two can be difficult. More recent and very interesting examples of superhumping LMXBs have included XTE J1118+480 (Uemura et al., 2000; Zurita et al., 2002) and GRS 1915+105 (Neil et al., 2007).

Another difference between CVs and LMXBs is that the mechanism for producing superhump light in CVs, enhanced heating of the disk by tidal stresses induced by the companion star, should not be important in LMXBs (Haswell et al., 2001). This is because the optical light should not be dominated by viscous dissipation, but instead by irradiation by X-rays. This suggests that instead the superhump arises from coupling of irradiation to tidal distortion of the disk. In support of this, Haswell et al. (2001) show that disk simulations do produce a $\sim 10\,\%$ increase in disk area at the time of superhump maximum. Smith et al. (2007) note that the period excess in LMXBs is also smaller than that in CVs and suggest that the precession period is longer because LMXB disks should be hotter and thicker due to irradiation.

The case of XTE J1118+480 is especially interesting. Superhumps were seen both during outburst, with varying morphology and period (Uemura et al., 2000), and late in the decay to quiescence (Zurita et al., 2002). The superhump periods inferred were just 0.1–0.6 % of the orbital period. Coupled with the extremely small mass ratio inferred spectroscopically (0.037 ± 0.007 Orosz 2001) this makes XTE J1118+480 an important object for studying the extreme limits of superhump behavior in which the 2:1 resonance may become the dominant mechanism for exciting disk eccentricity.

1.5.5 Super-orbital Periods

Other periods longer than the orbital period can arise. The most famous is the 35 day period seen in the neutron star LMXB Her X-1. This manifests in both a long modulation in optical light curve morpholo-

gies (Gerend and Boynton, 1976) and changes in X-ray pulse profiles. The optical behavior was modeled successfully with a precessing tilted accretion disk which modulates shadowing of the companion star on a 35 day period. The mechanism for inducing this tilt is now believed to be radiation-driven warping of the accretion disk (Wijers and Pringle, 1999).

Ogilvie and Dubus (2001) investigated the stability of accretion disks to radiation driven warping in systems of a wide range of mass ratios and binary separations. They focused on the two lowest order warping modes, 0 and 1, and identified several regimes where disks were either stable or unstable to mode-0 perturbations, to mode-1 perturbations, or to both. Reassuringly, Her X-1 lies in the region unstable to mode-0 only, and most other systems in the unstable regime also exhibit super-orbital periodicities of some form. Clarkson et al. (2003) tested this description more thoroughly with a dynamic power-spectral analysis of RXTE lightcurves. Systems such as Her X-1 and LMC X-4 which are in the pure mode-0 regime exhibit relatively stable periodicities. SMC X-1 which lies close to the region of mode-1 instability exhibits a less stable long period, whereas Cyg X-2 which is unstable to both mode-0 and mode-1 oscillations exhibits complex and multi-periodic behavior.

1.5.6 Quasi-Periodic Oscillations

Quasi-periodic oscillations, or QPOs, are common on many timescales in LMXBs. Some of the super-orbital periods discussed above would qualify as long-period QPOs rather than strict periodicities. At the other extreme of timescale there is a rich phenomenology of high frequency (milliseconds to seconds) QPO behavior seen in X-ray observations of LMXBs arising from the inner accretion flow. We will not discuss that here and focus on those QPOs visible in the optical and/or UV; for a review of X-ray QPOs see van der Klis (2006).

A QPO is a repeating signal that is not strictly periodic. It may wander in frequency or exhibit changes in phase. A transient signal, for example a decaying series of pulses, will also manifest as a QPO. In a Fourier transform, a QPO appears as a peak with finite width, whereas a true coherent periodicity has width limited only by the time-period sampled by the data. QPOs are often characterized by their coherence, $Q = \nu/\Delta\nu$, which is a measure of how broad the QPO is in frequency space. A low coherence QPO is essentially an excess of noise around a peak frequency, defining a preferred but not unique timescale.

One class of optical QPOs has been seen in two UCXBs now. Chakrabarty et al. (2001) identified a strong optical and UV QPO around 1 mHz in the 42 min orbital period system 4U 1626–67. This was seen to be moderately coherent ($Q \sim 8$) stronger in the UV than optical, and completely absent in X-rays. The authors attributed the effect to a precessing warp in the inner accretion disk. Subsequently a similar feature also around 1 mHz has been seen in 4U 0614+091 (Zhang et al., in preparation). This system is believed to have an orbital period of 51 min (Shahbaz et al., 2008b), so the similarity of timescales to 4U 1626–67 is striking.

A timescale around 1 mHz also appears to be significant in quiescent SXTs, although this is probably coincidence given the very different orbital periods and physical conditions. Hynes et al. (2003b) identified a break in the power-density spectrum of the 8 hr period system A 0620–00 at around 1 mHz. An actual QPO at 0.78 mHz was seen in the 6.5 day period V404 Cyg (Shahbaz et al., 2003) and at 2 mHz in the 4.1 hr system XTE J1118+480 (Shahbaz et al., 2005). The favored explanation for QPOs in quiescent SXTs has been that they are associated with the transition from a thin accretion disk to an evaporated advective flow, although the interpretation is probably not as simple as associating the QPO frequency with the Keplerian rotation period at the transition radius.

1.6 Spectroscopy

1.6.1 Emission and Absorption Line Spectra

Luminous X-ray binaries can show a range of emission lines, although their spectra are nowhere near as rich as those of planetary nebulae or active galactic nuclei can be. We show an example, the blue spectrum of Sco X-1, in Fig. 1.9. H I lines of the Balmer series in the optical and Brackett series in the infrared are common, but by no means ubiquitous. They can be absent, and sometimes show absorption structure. He I lines often accompany H I. More reliably present are He II lines in the optical (dominated by 4686 Å) and ultraviolet (1640 Å).

Besides hydrogen and helium, the main other lines seen are of carbon, nitrogen, oxygen, and silicon. In the optical the strongest of these features is a blend of N III and C III lines around 4640 Å commonly referred to as the Bowen blend (McClintock et al., 1975), but many weaker lines are present and can be seen in high quality spectra of Sco X-1 (Steeghs

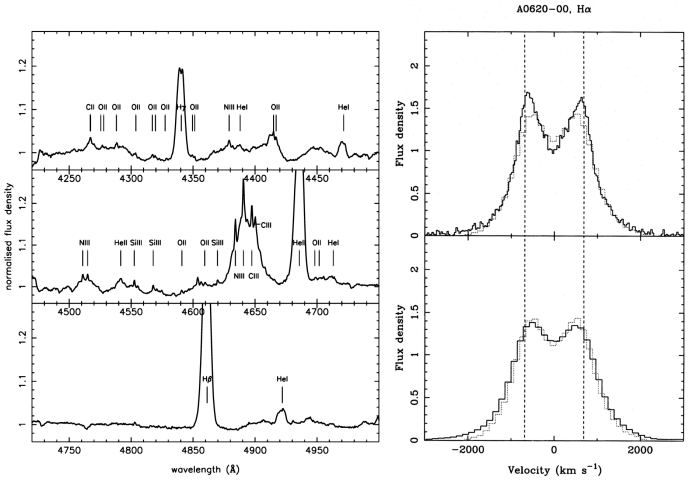

Figure 1.9 Left: Blue spectrum of Sco X-1 from Steeghs and Casares (2002). This shows the typical range of atomic emission lines present in the spectrum of a bright LMXB. Right: Hα profiles of A 0620–00 from Marsh et al. (1994). This illustrates the typical double-peaked disk profile especially seen in quiescent LMXBs. Solid data are that of Marsh, dotted is from Johnston et al. (1989). In the lower panel, Marsh's data has been binned at blurred to match that of Johnston. Dashed lines indicate the velocity of the outer edge of the disk inferred by Marsh.

and Casares, 2002). In the UV, several strong resonance lines dominate: C IV 1548,1551 Å, N V 1239,1243 Å, Si IV 1394,1403 Å, and O V 1371 Å are the most prominent. Dramatic differences in the relative intensities of these have been seen between objects with carbon and oxygen lines sometimes completely absent. This has been interpreted as evidence for CNO processing in the donor star (Haswell et al., 2002). Among ultra-compact systems, hydrogen, and sometimes even helium may be absent leaving spectra dominated by carbon and oxygen (Nelemans et al., 2004, 2006).

In quiescence, higher excitation lines of He II together with the CNO lines are absent, and only H I and very weak He I are present in emission. Provided the disk is sufficiently dim, the photospheric absorption spectrum of the companion emerges facilitating measurement of its radial velocity curve and rotational broadening and derivation of the system parameters. This will be discussed in Section 1.6.3.

1.6.2 Emission Line Profiles and Doppler Tomography

Quiescent LMXBs present the simplest emission line profiles to understand. Optical hydrogen and helium lines are seen with a double-peaked profile (e.g. Fig. 1.9) consistent with expectations from an approximately axisymmetric Keplerian accretion disk as also seen in CVs (Horne and Marsh, 1986). The blue wing of the profile comes from the side of the disk approaching us, and the red wing from that which is receding. Most sensitively, the peak separation can measure the velocity at the outer edge of the disk. More close examination, however, reveals changes in the line profiles, with the relative strengths of the two peaks varying. To examine how this relates to the binary orbital phase, it is usual to plot a trailed spectrogram, with wavelength (equivalent to velocity for a single line) on the x-axis and orbital phase on the y-axis. Good quality data then reveals that the asymmetries arise from a third peak moving back and forth sinusoidally, tracing out an S-wave in the trailed spectrum (e.g Fig. 1.10; Marsh et al. 1994).

To better understand how such components can be associated with locations in the binary, the technique of Doppler tomography has been developed. A number of documents have reviewed this well, for example Marsh (2001). The key idea is that any given component of the binary should have a defined velocity in the orbital plane that can be resolved into x and y components, V_x and V_y. Each such component will also lead to a single S-wave in a trailed spectrogram. Doppler tomography is essentially a transformation from visualizing the data in terms of radial velocity and phase to an alternative visualization in terms of V_x and V_y. Thinking of the $V_x - V_y$ plane in terms of polar coordinates, the phasing of an S-wave component dictates the azimuth of a spot in the $V_x - V_y$ plane, and its amplitude determines the distance of the point from the origin ($V_x = V_y = 0$). Doppler tomography can also be thought of as representing the trailed spectrogram as a sum of an arbitrary number of S-waves.

The dominant component that is expected in a Doppler tomogram is a ring of emission in velocity space corresponding to the accretion disk (see e.g. Fig. 1.10; Marsh et al. (1994)). Since this is represented in velocity space the inner disk has high velocities and so is on the outside of the ring in the tomogram; in this sense tomograms are inside-out compared to visualizing things in real space. The other component most often seen is a structure on the left hand side corresponding to the accretion stream, the stream-impact point, or a bulge in the disk downstream of it. In

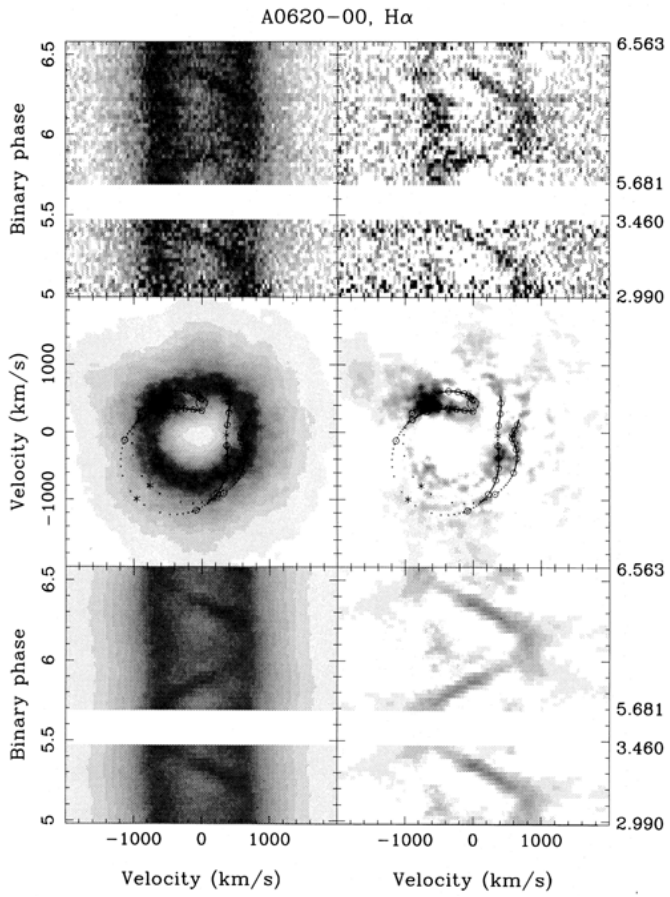

Figure 1.10 Doppler tomogram of Hα emission in A 0620–00 from Marsh et al. (1994). The right hand panels shows the effect of subtracting the non-varying part of the trailed spectrum (equivalent to the symmetric part of the tomogram. The upper panel shows the data, the middle is the tomogram, and the lower is a reconstruction of the data from the tomogram.

quiescent LMXBs such as A 0620–00 this is relatively well behaved and lies at velocities expected for the accretion stream (Marsh et al., 1994). In persistent LMXBs, however, the maximum emission often lies below the expected stream velocities in the tomogram (Casares et al., 2003; Pearson et al., 2006) and may even appear in the lower-left quadrant (Hynes et al., 2001). This is usually attributed to a bulge introduced

by the stream-impact or material overflowing the disk, but its origin is not yet fully understood. The final component sometimes revealed in some emission lines is the companion star. This will be discussed more in Section 1.6.4.

There are several limitations of the technique to keep in mind, especially as X-ray binaries can violate a number of these. Doppler tomography assumes that emission lines are optically thin and that all of the flux is visible all of the time. This requires lines that do not modulate in integrated intensity over the binary orbit, yet observationally such modulations usually are present, with eclipses presenting the most dramatic example. The new technique of modulation tomography (Steeghs, 2003) partially addresses this by allowing the line intensity to modulate sinusoidally. This technique has been successfully applied to the quiescent LMXB XTE J1118+480 by Calvelo et al. (2009), where it is found that the disk component, as expected, does not modulate in intensity but the accretion stream impact point does. Another limitation which can more justifiably be assumed satisfied is that all motions are in the plane (i.e. there is no V_z component). Even so, a disk wind, for example, violates this assumption and wind emission would confuse the reconstruction. A final thing to keep in mind, but not a limitation of the technique as such, is that a Doppler tomogram is reconstructed in velocity space, not real space. The velocities of emitting material can be constrained, but additional assumptions, such as system parameters, are required to associate these velocity components with physical components of the binary. Conversely, of course, this means that Doppler tomograms can be used to constrain those system parameters, and we will return to this idea in Section 1.6.4. Even knowing system parameters, the mapping between real and velocity space is not one-one, and so there may be ambiguity about the physical location of emitting material.

1.6.3 Mass Determinations in Quiescent Systems

Binary system parameters, and especially masses, are essential for many purposes. Specific parameters provide information about the evolutionary state of a system, while distributions in period and compact object mass, for example, test models for the formation and evolution of binary populations (Fryer and Kalogera, 2001; Pfahl et al., 2003). A compact object mass in excess of $3\,\mathrm{M}_\odot$ is considered the most convincing evidence for a black hole, while precise measurements of neutron star masses could constrain the equation of state of neutron star matter (e.g.

Özel and Psaltis 2009). Finally, most of the observational techniques described here depend, to a greater or lesser degree, on knowing the system parameters for a quantitative interpretation.

Dynamical parameter determinations are underpinned by Kepler's Third Law which can be expressed as:

$$f(M) = \frac{K_2^3 P_{\rm orb}}{2\pi G} = M_1 \frac{\sin^3 i}{(1+q)^2} \tag{1.6}$$

where K_2 is the radial velocity semi-amplitude of the donor star, $P_{\rm orb}$ is the binary orbital period, M_1 is the compact object mass, i is the binary inclination, and $q = M_2/M_1$ is the mass ratio. $f(M)$ is termed the mass function. It is of crucial importance because a) it can be measured from the radial velocity curve alone (K_2 and $P_{\rm orb}$) and b) it provides a strict lower limit on M_1 (since $\sin i \leq 1$ and $1 + q > 1$). Many objects have been classified as a black hole purely on the basis of mass functions greater than the assumed maximum mass of a neutron star around $3\,{\rm M}_\odot$. The most convincing example, and an excellent case-study for system parameter determination in general, is V404 Cyg (Casares et al., 1992; Casares and Charles, 1994). It has an orbital period of 6.47 days and $K_2 = 208.5 \pm 0.7\,{\rm km\,s^{-1}}$. This leads to a mass function $f(M) = 6.08 \pm 0.06\,{\rm M}_\odot$.

Beyond this, it can be seen that determination of the actual compact object mass requires measurement of the binary mass ratio and inclination. The preferred method to estimate the mass ratio is to observe rotational broadening in photospheric absorption lines from the donor star. Since the projected radial velocity semi-amplitude, K_2, and the rotational broadening, $v \sin i$, are both affected by orbital inclination in the same way, the ratio of $v \sin i / K_2$ is purely a function of the ratio of the radius of the donor star to the binary separation and hence is a function of q only (although details such as limb darkening are important for precise measurement of $v \sin i$ from observed rotationally broadened lines). A good approximation (see e.g. Wade and Horne 1988) is

$$V_{\rm rot} \sin i = 0.462 K_2 q^{1/3} (1+q)^{2/3}. \tag{1.7}$$

In practice, rotational broadening measurements are challenging since the expected values, typically below $100\,{\rm km\,s^{-1}}$, are often close to the spectral resolution of the data used. The usual method to extract this information is to observe both the target and a template star of matched spectral type and then convolve the template spectrum with rotational broadening profiles until an optimal match is found. In the case of

V404 Cyg, Casares and Charles (1994) measured $V_{\rm rot} \sin i = 39.1 \pm 1.2\,{\rm km\,s^{-1}}$ which, together with K_2 cited above, yields $q = 0.060^{+0.004}_{-0.005}$.

An alternative approach to the mass ratio is to attempt to measure the radial velocity semi-amplitude of the compact object, K_1, from disk emission lines, since $q = K_1/K_2$. In practice this has been fraught with errors, with emission line radial velocity curves exhibiting incorrect phasings and different systemic velocities to the companion star. It is argued that these effects arise from asymmetries far out in the disk, and that they can be minimized by measuring just the high velocity wings of a line, but even then, mass ratios from rotational broadening are preferable.

The preferred method to determine the inclination would be to model eclipses (see Section 1.5.3). Most systems (including all Galactic black hole candidates) do not eclipse, however, so instead the usual method has been to measure ellipsoidal variations (see Section 1.5.1). Continuing our case-study of V404 Cyg, the ellipsoidal variation study of Shahbaz et al. (1994) is illustrated in Fig. 1.8. These authors model IR ellipsoidal modulations to deduce $i = 56 \pm 4^\circ$. Combined with the mass function and mass ratio measurements discussed above, this implies $10\,{\rm M}_\odot < M_1 < 15\,{\rm M}_\odot$ with a preferred value of $M_1 = 12\,{\rm M}_\odot$. As discussed in Section 1.5.1, an important concern with ellipsoidal studies is that the modulations may be diluted by disk contamination. Shahbaz et al. (1996) measured this in the IR and placed an upper limit on the disk contribution of 14 %. This at most reduces the derived mass by $2\,{\rm M}_\odot$ from $12\,{\rm M}_\odot$ to $10\,{\rm M}_\odot$.

It should be emphasised that we have focused on V404 Cyg because it is both one of the best studied systems, and one with the cleanest results. In most quiescent SXTs, measurements are less precise and concerns about disk contamination are more serious, and consequently most mass determinations in these systems are much less secure. This method has now been applied to about 15 quiescent SXTs. For a recent compilation, see Casares (2007).

1.6.4 Mass Determinations in Luminous Systems

As the accretion rate increases from quiescence, the optical light quickly becomes dominated by the heated accretion disk and companion star. This means that in most persistently luminous LMXBs, we never have the opportunity to perform a radial velocity study of photospheric absorption lines from the unheated portions of the companion. There are a few exceptional systems in which the donor star is a giant and is still

visible even in luminous states. Cyg X-2 is the most famous example (Casares et al., 1998) and 2S 0921–636 is another (Shahbaz et al., 2004; Jonker et al., 2005).

In other systems we must seek a different source of radial velocity information. A new approach was suggested by observations of Sco X-1 which revealed narrow emission components in the Bowen blend (see Section 1.6.1) that moved in anti-phase with broader components attributed to the disk (Steeghs and Casares, 2002). The radial velocity curve of just the sharp components yielded $K_2 > 77\,\mathrm{km\,s^{-1}}$ and the authors derived a neutron star mass $\sim 1.4\,\mathrm{M}_\odot$, consistent with that usually expected. The major caveat here is that the emission lines would originate from the heated inner face of the donor star, and so their center-of-light would not coincide with the donor's center of mass. This is why the K_2 value derived by this method is only a lower-limit on the true value. To improve on this requires modeling of the binary geometry to attempt to estimate by how much K_2 is underestimated (Muñoz-Darias et al., 2005).

Sco X-1 was an ideal case. Only one other system, the long-standing black hole candidate GX 339–4, has shown clear, sharp, moving N III and C III components in individual spectra (Hynes et al., 2003a). These observations provided both a convincing orbital period of 1.76 days, and a mass function of $f(M) = 5.8 \pm 0.5\,\mathrm{M}_\odot$, finally confirming the black hole nature of this source. In other objects, such as 2A 1822–371, sharp components cannot be identified in the line profiles directly, but the companion star can be picked out very effectively using Doppler tomography (Casares et al., 2003). For a more complete review of what has been achieved by this method, see Cornelisse et al. (2008).

1.7 Rapid Variability

1.7.1 Echo-Mapping

Multiwavelength variability is a near universal characteristic of X-ray binaries. X-rays vary due to rapid changes in the inner accretion flow on timescales of milliseconds and longer. These X-rays then irradiate the outer accretion disk and companion star, resulting in reprocessed optical and UV radiation which is expected to be imprinted with the same variability as the X-ray signal. An important difference, however, is that the optical emission and X-rays originate from a volume of significant spatial extent, resulting in light travel time delays between the

X-rays and the reprocessed emission. It is then possible to infer information about the geometry and scale of the reprocessing region from the lags measured between X-ray and optical/UV variability; this technique is known as reverberation or echo-mapping, as the reprocessed light behaves as an echo. Echo or reverberation mapping is not uniquely applied to X-ray binaries. Much of the development and application of the technique has been for active galactic nuclei (AGN); see for example Peterson and Horne (2006) for a recent review of the AGN problem, and O'Brien et al. (2002) for the application to X-ray binaries.

The key idea is that local optical (or UV) variability, in either lines or continuum, is induced by reprocessing of X-ray variability, but with a lag varying with reprocessing location. Each such location can be thought of as responding to X-rays with a delta-function response at a delay time determined by the path difference between direct and reprocessed emission. The total optical response is then the sum of lagged responses from all the reprocessing elements. For a delta-function variation in the X-rays the optical response is then termed the transfer function, and measures how strong the response is as a function of the delay, effectively encoding information about the reprocessing geometry. For continuously variability, the optical lightcurve can be modeled as a convolution of the X-ray lightcurve with the transfer function:

$$L_{\rm opt}(t) = L_{\rm X} * \Psi = \int L_{\rm X}(t-\tau)\Psi(\tau)d\tau \tag{1.8}$$

where $L_{\rm X}$ and $L_{\rm opt}$ are the X-ray and optical luminosities, Ψ is the transfer function, and τ is the X-ray to optical lag.

Several assumptions are inherent in this description. It is assumed that the optical responds linearly to the X-rays, or at least that a non-linear response can be linearized for small perturbations. It is also implicit that the X-rays originate from a point source, or at least a region much smaller in spatial extent than the reprocessing region. Finally, to determine geometric information it is necessary that the lags be geometric in origin; significant reprocessing times would compromise this.

Geometrical modeling of the response

In the case of X-ray binaries, we have a clearer expectation of the reprocessing geometry than in AGN. We anticipate reprocessing from the accretion disk around the compact object, possibly enhanced at a bulge where material feeds into the disk from the companion star. We also might expect some reprocessing from the heated inner face of the com-

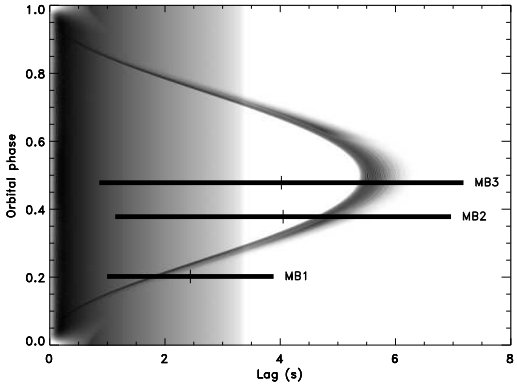

Figure 1.11 Strength of response (indicated by grayscale) as a function of orbital phase and lag, as calculated by the binary modeling code of O'Brien et al. (2002). Solid bands indicate the ranges of lags inferred from X-ray bursts by Hynes et al. (2006b) for EXO 0748–676.

panion star. O'Brien et al. (2002) and Muñoz-Darias et al. (2005) modeled the reprocessing geometry to predict transfer functions for a variety of binary parameters. An example as a function of orbital phase is shown in Fig. 1.11. Simplistically, one expects two components. The disk will extend from zero lag to $r_{\rm disk}(1+\sin i)$ where $r_{\rm disk}$ is the disk radius in light seconds and i the binary inclination. Within this range the shape of the response is strongly sensitive to the inclination and somewhat less so to the degree of disk flaring. The response from the companion star approximately oscillates within the range $a(1\pm\sin i)$ over the course of the binary orbit, where a is the binary separation in light seconds. The strength and width of the companion response is a strong function of the mass ratio and disk thickness (which determines how much of the companion is shielded). One of the great appeals of applying echo-mapping to X-ray binaries is that with phase-resolved observations of the companion echo over the orbit, one could measure both a and i independently of other techniques and assumptions.

Empirical descriptions of the response

Many echo-mapping studies use more pragmatic, and less model-dependent approaches. Ideally, one would take high quality X-ray and optical lightcurves and deconvolve them to directly determine the shape of the transfer function. This is the basis of the maximum entropy echo-mapping technique

(Horne, 1994) in which a maximum entropy regularization method is used to suppress the problem of fitting the noise. Unfortunately, typical X-ray binary datasets do not have the signal-to-noise ratio for this to work effectively.

A simpler approach has been developed in which a very simple functional form is adopted for the transfer function, either a rectangular response (Pedersen et al., 1982) or a Gaussian (Hynes et al., 1998). Both are introduced as approximations to the response rather than for a physically motivated reason, and amount to the assumption that the data only constrain the mean lag and the amount of smearing out in time of the variability. The Gaussian formulation essentially yields the first two moments of the delay distribution. There is a potential difficulty with this approach as noted by Muñoz-Darias et al. (2007). If the X-ray lightcurve is convolved with a Gaussian this smooths the data and has the effect of suppressing the noise. If the noise in the X-ray lightcurve is significant compared to the real variability (or if there is additional variability that does not correlate with that in the optical) then the χ^2 of a fit may be reduced by adopting an artificially high Gaussian width, i.e. over-smoothing the data. Thus there is a possibility that the widths of transfer functions derived in this way may be over-estimated.

An even simpler, but widely used approach is to measure the cross-correlation function (CCF) of the two datasets, defined for continuously sampled data as:

$$\mathrm{CCF}(\tau) = \frac{\int [f(t) - \bar{f}][g(t+\tau) - \bar{g}]}{\sigma_f \sigma_g} \tag{1.9}$$

where f and g are the driver and echo time-series respectively, $\bar{f}$ and $\bar{g}$ are their means, σ_f and σ_g are their standard deviations, and τ is the lag at which the CCF is being evaluated. Gaskell and Peterson (1987) and Edelson and Krolik (1988) discuss two approaches to implementing this calculation for discretely and unevenly sampled data. This yields an estimate of the mean lag but information about the smearing is hard to extract, and care should be taken in interpreting the results of a cross-correlation analysis (Koen, 2003). If the driver-echo relationship is accurately described by the convolution in equation 1.8 then the CCF is equivalent to the driver auto-correlation function (ACF) convolved with the transfer function. In cases where the driver ACF is relatively narrow, the CCF may provide a reasonable approximation to the transfer function. We show an example in Fig. 1.12, based on X-ray/optical data from the black hole transient Swift J1753.5–0127 (Hynes et al., 2009a).

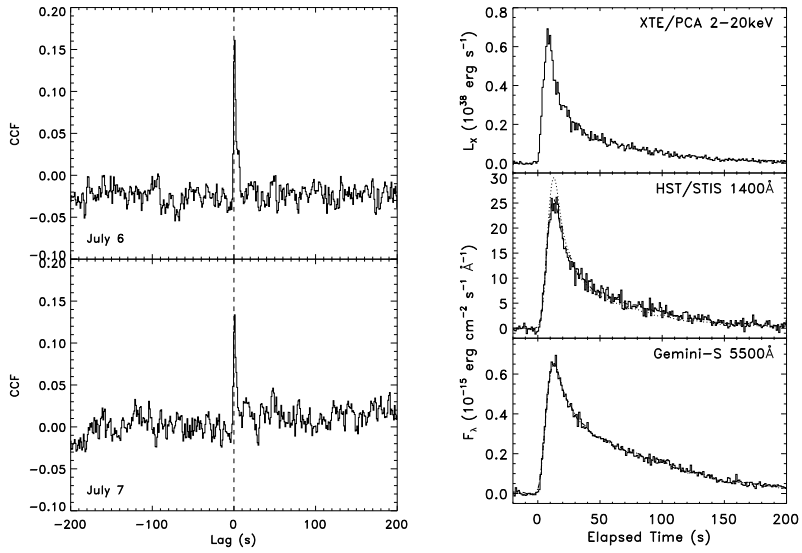

Figure 1.12 Left: X-ray/optical cross-correlations of Swift J1753.5–0127 early in outburst, from Hynes et al. (2009a). Right: Simultaneous burst profiles in EXO 0748–676 from Hynes et al. (2006b). Dotted lines assume fixed normalization of the UV flux relative to the optical, solid line fits allow this normalization to float.

1.7.2 Type I X-ray Bursts

Type-I X-ray bursts are thermonuclear explosions on the surface of a neutron star in an LMXB (Strohmayer and Bildsten, 2006). They represent an enormous increase in the X-ray flux, a factor of twenty or more in lower luminosity systems, rising on a timescale of a few seconds. X-ray bursts then have the potential to be an ideal echo-mapping probe. Hence it is using these events that some of the first echo-mapping experiments were performed. Reprocessed optical bursts were discovered in the late 1970's in the LMXBs 4U 1735–444 and Ser X-1 (Grindlay et al., 1978; McClintock et al., 1979; Hackwell et al., 1979). The optical flux was found to rise by nearly a factor of two and lag a few seconds behind the X-rays. It was immediately appreciated that the optical flux was several orders of magnitude too high to be due to direct emission from the neutron star surface, and hence that the brightening must be due to reprocessing of X-rays by the much larger projected area of the accretion disk and/or companion star. The 2.8 s lag in 4U 1735–444

(McClintock et al., 1979) supported this interpretation, being consistent with the expected light travel time delays in this short-period binary.

The large amplitudes of X-ray bursts drive a stronger optical response than X-ray flickering does, and so provide additional information not available when variability is a small perturbation. Observations never record the total bolometric luminosity, but always that within a specific bandpass. Consequently the shape of the observed reprocessed lightcurve depends on the spectral evolution as the reprocessor cools and the peak of the spectrum moves into or out of the bandpass used. Shorter wavelengths are sensitive to hotter material, they are expected to decay more rapidly, and hence multicolor observations of X-ray bursts provide some temperature sensitivity, in addition to that lag information which is available even for smaller perturbations. This is not a subtle effect, and the early observations indicate the reprocessor temperature typically doubles during a burst (Lawrence et al., 1983).

The best dataset for the method yet obtained was obtained for EXO 0748–676 (Hynes et al., 2006b). Four bursts were observed over two successive nights using RXTE and Gemini-S, providing some phase information, and one of these was also observed at high time-resolution in the far-UV by *HST*/STIS (Fig. 1.12). The latter was a unique observation to date, providing far more sensitivity to high temperature responses than is possible with optical data alone, and also yielding a time-resolved UV spectrum, facilitating a direct test of the expectation that the reprocessed light should be close to a black body. Perhaps most interestingly, the three bursts observed sampled enough of a phase range to see apparent changes in the lag and smearing as a function of orbital phase (Fig. 1.11). The phasing and amplitude of the changes seen are both consistent with expectations of models in which both the disk and the companion star contribute to reprocessing. This is one of the few observations to date that can claim to be true echo-tomography exploiting different viewing angles of the binary.

1.7.3 Flickering in Persistent Neutron Star Systems

While bursts provide an ideal signal for echo-mapping in some neutron star binaries, we must seek another technique in black hole systems and non-bursting neutron stars. An alternative source of variability is provided by the flickering that seems a ubiquitous signature of accretion. Since this flickering is always present at some level, unlike bursts which only recur every few hours, flickering variability can potentially provide

phase-resolved information in any system. This potential has yet to be fully realized, however. It has been found that the optical response is rather weak, with standard deviations of only a few percent in the optical lightcurves. Consequently, high signal-to-noise observations are needed to pick out a measurable correlation. Even then, success is typically only achieved when high levels of variability are present, with other datasets yielding a non-detection.

There are several bright and persistently active neutron star X-ray binaries that potentially provide ideal targets for these studies. It is in fact somewhat surprising that more has not yet been achieved with these. The bright neutron star system Sco X-1 was observed by Ilovaisky et al. (1980) and Petro et al. (1981). Both found correlations, with evidence for lags and substantial smearing of the response; Petro et al. (1981) described the optical response as a low-pass filtered version of the X-rays, with variability on timescales < 20 s smoothed out. McGowan et al. (2003) reanalyzed these datasets with the Gaussian transfer function method. In some cases, no good fit could be obtained. The pair of lightcurves where the method did appear to succeed yielded a lag of 8.0 ± 0.8 s and Gaussian dispersion of 8.6 ± 1.3 s. For comparison, lags of up to 4–5 s are expected from the disk and 10 s from the companion star.

We recently obtained some superb quality observations of Cyg X-2. Very clear correlations were seen when the source was on the flaring branch. A Gaussian transfer function analysis of the whole lightcurve proved unsatisfactory as we see not only a modulation of the optical light that is absent in X-rays, but also an apparent variation in the efficiency of reprocessing from one event to the next. Much more success was achieved by analyzing individual events in the lightcurve independently. A Gaussian fit to the transfer function then suggests lags around 10 s, as might be expected from the accretion disk in this long-period (9.8 day) binary. The data quality are sufficient to permit direct comparison with model transfer functions as well. We show in Fig. 1.13 a small segment of the optical lightcurve with fits generated by convolving the X-ray lightcurve with model transfer functions generated using the code of O'Brien et al. (2002), and parameters from Casares et al. (1998) and Orosz and Kuulkers (1999). The relative contribution of reprocessing from disk and companion star is highly sensitive to the amount of shielding of the companion by the disk, hence we have considered the two components separately. The data appear much more consistent with the pure disk model than the pure companion star model suggesting that

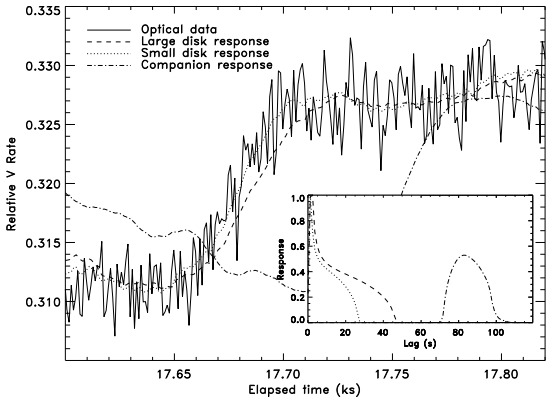

Figure 1.13 Fit to optical data for Cyg X-2 in the flaring branch. The dashed line shows the response from the whole disk, the dotted line is that from just the inner disk, and the dash-dot line is from the companion star.

the disk (and indeed just the inner disk) dominates the response, at least in the optical continuum.

Muñoz-Darias et al. (2007) tried a different approach on Sco X-1. As discussed in Section 1.6.4, we have realized in recent years that the Bowen blend of N III and C III lines around 4640 Å often contain a strong component from the companion star. They used a narrow-band filter encompassing the Bowen blend and He II 4686 Å to attempt emission line echo-mapping. They report results from several flaring branch data segments showing strong correlated variability. As expected, they find longer lags from the narrow-band filter containing the Bowen blend than from a continuum bandpass, suggesting that the Bowen response contains a larger contribution from the companion star. After attempting to remove the continuum contribution from the Bowen lightcurves, they estimate a line lag of $\tau_0 = (13.5 \pm 3.0)$ s and a continuum lag of $\tau_0 = (8.5 \pm 1.0)$ s. The difficulty of continuum subtraction with narrow-band photometry is a limitation of this approach and we can expect a significant improvement with rapid spectroscopy with new instrumentation such as ULTRASPEC (Dhillon et al., 2008).

1.7.4 Another Mechanism for Correlations?

Fundamental to echo-mapping is the assumption that correlated X-ray and optical/UV variability indicate reprocessing of the X-rays by relatively cool material. We should not take this for granted, however, and there are some observations which seriously challenge this assumption.

The first indication of difficulties came from fast optical observations of the black hole binary GX 339–4 (Motch et al., 1982, 1983). Dramatic optical variability was seen extending to extremely short timescales (10–20 ms), much shorter than the light travel timescales expected, or the smearing typically observed in other systems described above. Fabian et al. (1982) argued that the flares most likely originated in cyclotron radiation, with a brightness temperature $> 9 \times 10^8$ K. Correlations were seen in a short (96 s) simultaneous observation, but of a puzzling nature. The X-ray and optical were anti-correlated with optical dips apparently preceding the X-rays by a 2.8 ± 1.6 s. The connection between X-ray and optical behavior was further reinforced by the presence of quasi-periodic oscillations at the same frequency in both energy bands. The brevity of the simultaneous observation, and the ambiguity in the lags introduced by quasi-periodic variability left this result tantalizing however.

New light was shed on this behavior by the 2000 outburst of the black hole system XTE J1118+480. A much larger time-resolved database was accumulated on this object including both simultaneous X-ray/optical data (Kanbach et al., 2001) and independent multi-epoch simultaneous X-ray/UV observations (Hynes et al., 2003c). Large amplitude X-ray variability was present, and accompanied by correlated optical and UV variations. In this case, a positive correlation with the optical/UV lagging the X-rays was clearly present, leading to hopes that this would be an ideal echo-mapping dataset. There were serious problems with this interpretation, however. These were most pronounced in the optical data (Kanbach et al., 2001) and included an optical auto-correlation function narrower than that seen in X-rays, and a cross-correlation function containing a marked "precognition dip" before the main peak. The latter could be interpreted in terms of optical dips leading X-ray flares by a few seconds, as suggested in GX 339–4, suggesting a common origin. Neither of these effects are expected in a reprocessing model. Light travel times should only act to smooth out optical responses, and hence broaden the optical auto-correlation function. Also, the continuum responses (as considered here) should generally be positively correlated with the X-rays, not anti-correlated. As in GX 339–4 the variability ex-

tended to very short timescales (< 100 ms) and hence Kanbach et al. (2001) estimated a minimum brightness temperature of 2×10^6 K. They also suggested that the strange variability properties were the result of optical cyclosynchrotron emission. These properties become weaker at shorter wavelengths (Hynes et al., 2003c), as does the variability, as might be expected if the behavior originates from a very red source of emission like synchrotron.

Dominant synchrotron emission in this system was not uniquely suggested by the variability properties. The very flat UV to near-IR spectrum had previously been attributed to synchrotron emission (Hynes et al., 2000) and the broad-band spectral energy distribution has been successfully accounted for using a simple jet model (Markoff et al., 2001). Striking support for a synchrotron origin for the variability has been provided by time-resolved IR observations during the 2005 outburst of XTE J1118+480 (Hynes et al., 2006a). Simultaneous 2 s images in the IR J, H, and K filters could be used to isolate the color of the IR variability. It was found to be very red ($F_\nu \propto \nu^{-0.78}$), consistent with optically thin synchrotron emission.

These arguments together provide strong evidence that a jet, or at least some kind of outflow, is responsible for much of the IR and even optical emission in XTE J1118+480 and for the correlated variability. By extension, the same interpretation may apply to other objects showing similar properties. GX 339–4 is of course a prime candidate and recent more extensive observations of this object show similar behavior (Gandhi et al., 2008). A third object has been added to the sample in Swift J1753.5–0127 (Durant et al., 2008; Hynes et al., 2009a). Here early observations near the outburst peak supported a simple reprocessing interpretation (Figure 1.12), with a transfer function consistent with the inferred system parameters, but later observations showed both negative and positive correlations rather similar to those in XTE J1118+480. The full explanation for the observed correlations and anti-correlations remains to be established, but this case illustrates that new astrophysics can be uncovered in unexpected places.

1.8 Conclusion

X-ray binaries emit across the electromagnetic spectrum, and a full understanding of accretion processes in this environment depends on multiwavelength observations. Not only do different wavelengths illuminate

different aspects of the behavior (inner disk, outer disk, companion star, jet, etc), but also connections between the different wavelengths provide essential information on causal connections between them. Understanding X-ray binaries to the fullest extent possible requires knowledge of not only X-ray and gamma-ray astronomy, but also optical, ultraviolet, infrared, and radio wavelengths.

1.9 Acknowledgements

I am grateful to the Instituto de Astrofísica de Canarias for the invitation and funding to present a series of lectures at the 21st IAC Winter School, on which this work is based. I would also like to gratefully acknowledge Valerie Mikles, Chris Britt, Lauren Gossen, and Chris Dupuis for providing an abundance of helpful comments on this manuscript and catching many mistakes in earlier versions. This is the document I would like to have given them when they began working in this field. Preparation of this work has made extensive use of NASA's Astrophysics Data System.

1.10 Glossary of Objects Cited

2A 1822–371: Persistent eclipsing neutron star LMXB. ADC source.
2S 0921–630: Persistent eclipsing neutron star LMXB. ADC source. Long period.
4U 0614+091: Persistent neutron star UCXB.
4U 1626–67: Persistent neutron star UCXB.
4U 1735-44: Persistent neutron star LMXB.
4U 1915–05: Persistent neutron star UCXB. Prototypical dipping source.
4U 2129+47: Quasi-persistent eclipsing neutron star LMXB. ADC source.
A 0620–00: Prototypical transient black hole LMXB.
Cir X-1: Persistent neutron star IMXB or HMXB. Eccentric orbit. Microquasar.
Cyg X-2: Persistent neutron star LMXB. Long period
EXO 0748–676: Quasi-persistent eclipsing neutron star LMXB.
GRO J0422+32: Transient black hole LMXB.
GRO J1655–40: Recurrent transient black hole IMXB. Microquasar.

GRS 1915+105: Quasi-persistent black hole LMXB. Microquasar. Very long period.
GS 2000+250: Transient black hole LMXB.
GX 339–4: Recurrent transient black hole LMXB.
Her X-1: Persistent eclipsing neutron star IMXB. Prototypical warped disk source.
LMC X-4: Persistent neutron star HMXB.
M33 X-7: Extragalactic eclipsing black hole HMXB.
Sco X-1: Persistent prototypical neutron star LMXB. First extra-solar X-ray source discovered. Brightest persistent extra-solar X-ray source in the sky.
Ser X-1: Persistent neutron star LMXB.
SMC X-1: Persistent neutron star HMXB.
Swift J1753.5–0127: Transient or quasi-persistent black hole LMXB.
X-ray Nova Muscae 1991: Transient black hole LMXB.
V404 Cygni: Transient black hole LMXB. Long period.
XTE J1118+480: Recurrent transient black hole LMXB.
XTE J1859+226: Transient black hole candidate LMXB.
XTE J2123–058: Transient eclipsing neutron star LMXB.

1.11 Glossary of Acronyms

ACF	Auto-correlation function
ADC	Accretion disk corona
AGN	Active galactic nucleus
BATSE	Burst And Transient Source Experiment (on board CGRO)
BHXRT	Black hole X-ray transient
CCF	Cross-correlation function
CGRO	Compton Gamma-ray Observatory
CV	Cataclysmic variable
DIM	Disk instability model
DN	Dwarf nova
FRED	Fast rise exponential decay
HMXB	High-mass X-ray binary
HST	Hubble Space Telescope
IMXB	Intermediate-mass X-ray binary
IR	Infrared
IUE	International Ultraviolet Explorer
LMXB	Low-mass X-ray binary

QPO	Quasi-periodic oscillation
RXTE	Rossi X-ray Timing Explorer
SED	Spectral Energy Distribution
STIS	Space Telescope Imaging Spectrograph (on board HST)
SXT	Soft X-ray transient
UCXB	Ultracompact X-ray binary
UV	Ultraviolet

References

Andrew, B. H., and Purton, C. R. 1968. Detection of Radio Emission from Scorpio X-1. *Nature*, **218**, 855–856.

Augusteijn, T., Kuulkers, E., and Shaham, J. 1993. 'Glitches' in soft X-ray transients: Echoes of the main burst? *A&A*, **279**, L13–L16.

Bayless, A. J., Robinson, E. L., Hynes, R. I., Ashcraft, T. A., and Cornell, M. E. 2010. The Structure of the Accretion Disk in the Accretion Disk Corona X-ray Binary 4U 1822–371 at Optical and Ultraviolet Wavelengths. *ApJ*, **709**, 251–262.

Blandford, R. D., and Konigl, A. 1979. Relativistic jets as compact radio sources. *ApJ*, **232**, 34–48.

Bradley, C. K., Hynes, R. I., Kong, A. K. H., Haswell, C. A., Casares, J., and Gallo, E. 2007. The Spectrum of the Black Hole X-Ray Nova V404 Cygni in Quiescence as Measured by XMM-Newton. *ApJ*, **667**, 427–432.

Brocksopp, C., Bandyopadhyay, R. M., and Fender, R. P. 2004. "Soft X-ray transient" outbursts which are not soft. *New Astronomy*, **9**, 249–264.

Brown, E. F., and Cumming, A. 2009. Mapping Crustal Heating with the Cooling Light Curves of Quasi-Persistent Transients. *ApJ*, **698**, 1020–1032.

Calvelo, D. E., Vrtilek, S. D., Steeghs, D., Torres, M. A. P., Neilsen, J., Filippenko, A. V., and González Hernández, J. I. 2009. Doppler and modulation tomography of XTEJ 1118+480 in quiescence. *MNRAS*, **399**, 539–549.

Cannizzo, J. K., Chen, W., and Livio, M. 1995. The Accretion Disk Limit Cycle Instability in Black Hole X-Ray Binaries. *ApJ*, **454**, 880–894.

Cantrell, A. G., Bailyn, C. D., McClintock, J. E., and Orosz, J. A. 2008. Optical State Changes in the X-Ray-quiescent Black Hole A0620-00. *ApJL*, **673**, L159–L162.

Casares, J. 2007. Observational evidence for stellar-mass black holes. Pages 3–12 of: V. Karas & G. Matt (ed), *IAU Symposium*. IAU Symposium, vol. 238.

Casares, J., and Charles, P. A. 1994. Optical studies of V404 Cyg, the X-ray transient GS 2023+338. IV. The rotation speed of the companion star. *MNRAS*, **271**, L5–L9.

Casares, J., Charles, P. A., and Naylor, T. 1992. A 6.5-day periodicity in the recurrent nova V404 Cygni implying the presence of a black hole. *Nature*, **355**, 614–617.

Casares, J., Charles, P. A., and Kuulkers, E. 1998. The Mass of the Neutron Star in Cygnus X-2 (V1341 Cygni). *ApJL*, **493**, L39–L42.

Casares, J., Steeghs, D., Hynes, R. I., Charles, P. A., and O'Brien, K. 2003. Bowen Fluorescence from the Companion Star in X1822-371. *ApJ*, **590**, 1041–1048.

Chakrabarty, D., Homer, L., Charles, P. A., and O'Donoghue, D. 2001. Millihertz Optical/Ultraviolet Oscillations in 4U 1626-67: Evidence for a Warped Accretion Disk. *ApJ*, **562**, 985–991.

Chen, W., Livio, M., and Gehrels, N. 1993. The secondary maxima in black hole X-ray nova light curves - Clues toward a complete picture. *ApJL*, **408**, L5–L8.

Chen, W., Shrader, C. R., and Livio, M. 1997. The Properties of X-Ray and Optical Light Curves of X-Ray Novae. *ApJ*, **491**, 312–338.

Cheng, F. H., Horne, K., Panagia, N., Shrader, C. R., Gilmozzi, R., Paresce, F., and Lund, N. 1992. The Hubble Space Telescope observations of X-ray Nova Muscae 1991 and its spectral evolution. *ApJ*, **397**, 664–673.

Clarkson, W. I., Charles, P. A., Coe, M. J., and Laycock, S. 2003. Long-term properties of accretion discs in X-ray binaries - II. Stability of radiation-driven warping. *MNRAS*, **343**, 1213–1223.

Corbel, S., and Fender, R. P. 2002. Near-Infrared Synchrotron Emission from the Compact Jet of GX 339-4. *ApJL*, **573**, L35–L39.

Corbet, R. H. D., Sokoloski, J. L., Mukai, K., Markwardt, C. B., and Tueller, J. 2008. A Comparison of the Variability of the Symbiotic X-Ray Binaries GX 1+4, 4U 1954+31, and 4U 1700+24 from Swift BAT and RXTE ASM Observations. *ApJ*, **675**, 1424–1435.

Cornelisse, R., Casares, J., Muñoz-Darias, T., Steeghs, D., Charles, P., Hynes, R., O'Brien, K., and Barnes, A. 2008 (May). An Overview of the Bowen Survey: Detecting Donor Star Signatures in Low Mass X-ray Binaries. Pages 148–152 of: R. M. Bandyopadhyay, S. Wachter, D. Gelino, & C. R. Gelino (ed), *A Population Explosion: The Nature & Evolution of X-ray Binaries in Diverse Environments*. American Institute of Physics Conference Series, vol. 1010.

Dhillon, V. S., Marsh, T. R., Copperwheat, C., Bezawada, N., Ives, D., Vick, A., and O'Brien, K. 2008. ULTRASPEC: High-speed spectroscopy with zero readout noise. Pages 132–139 of: D. Phelan, O. Ryan, & A. Shearer (ed), *High Time Resolution Astrophysics: The Universe at Sub-Second Timescales*. American Institute of Physics Conference Series, vol. 984.

Dubus, G., Lasota, J.-P., Hameury, J.-M., and Charles, P. 1999. X-ray irradiation in low-mass binary systems. *MNRAS*, **303**, 139–147.

Dubus, G., Hameury, J.-M., and Lasota, J.-P. 2001. The disc instability model for X-ray transients: Evidence for truncation and irradiation. *A&A*, **373**, 251–271.

Durant, M., Gandhi, P., Shahbaz, T., Fabian, A. P., Miller, J., Dhillon, V. S., and Marsh, T. R. 2008. Swift J1753.5-0127: A Surprising Optical/X-Ray Cross-Correlation Function. *ApJL*, **682**, L45–L48.

Edelson, R. A., and Krolik, J. H. 1988. The discrete correlation function - A new method for analyzing unevenly sampled variability data. *ApJ*, **333**, 646–659.

Esin, A. A., McClintock, J. E., and Narayan, R. 1997. Advection-dominated Accretion and the Spectral States of Black Hole X-Ray Binaries: Application to Nova Muscae 1991. *ApJ*, **489**, 865–889.

Fabian, A. C., Guilbert, P. W., Motch, C., Ricketts, M., Ilovaisky, S. A., and Chevalier, C. 1982. GX 339-4 - Cyclotron radiation from an accretion flow. *A&A*, **111**, L9–L10.

Fender, R. P., Gallo, E., and Jonker, P. G. 2003. Jet-dominated states: an alternative to advection across black hole event horizons in 'quiescent' X-ray binaries. *MNRAS*, **343**, L99–L103.

Fitzpatrick, E. L. 1999. Correcting for the Effects of Interstellar Extinction. *PASP*, **111**, 63–75.

Frank, J., King, A., and Raine, D. J. 2002. *Accretion Power in Astrophysics: Third Edition*. Cambridge University Press.

Froning, C. S., Robinson, E. L., and Bitner, M. A. 2007. Near-Infrared Spectra of the Black Hole X-Ray Binary A0620-00. *ApJ*, **663**, 1215–1224.

Fryer, C. L., and Kalogera, V. 2001. Theoretical Black Hole Mass Distributions. *ApJ*, **554**, 548–560.

Gallo, E., Fender, R. P., and Hynes, R. I. 2005. The radio spectrum of a quiescent stellar mass black hole. *MNRAS*, **356**, 1017–1021.

Gallo, E., Migliari, S., Markoff, S., Tomsick, J. A., Bailyn, C. D., Berta, S., Fender, R., and Miller-Jones, J. C. A. 2007. The Spectral Energy Distribution of Quiescent Black Hole X-Ray Binaries: New Constraints from Spitzer. *ApJ*, **670**, 600–609.

Gandhi, P., Makishima, K., Durant, M., Fabian, A. C., Dhillon, V. S., Marsh, T. R., Miller, J. M., Shahbaz, T., and Spruit, H. C. 2008. Rapid optical and X-ray timing observations of GX 339-4: flux correlations at the onset of a low/hard state. *MNRAS*, **390**, L29–L33.

Gaskell, C. M., and Peterson, B. M. 1987. The accuracy of cross-correlation estimates of quasar emission-line region sizes. *ApJS*, **65**, 1–11.

Gelino, D. M., Harrison, T. E., and Orosz, J. A. 2001. A Multiwavelength, Multiepoch Study of the Soft X-Ray Transient Prototype, V616 Monocerotis (A0620-00). *AJ*, **122**, 2668–2678.

Gerend, D., and Boynton, P. E. 1976. Optical clues to the nature of Hercules X-1/HZ Herculis. *ApJ*, **209**, 562–573.

Giacconi, R., Gursky, H., Paolini, F. R., and Rossi, B. B. 1962. Evidence for x Rays From Sources Outside the Solar System. *Physical Review Letters*, **9**, 439–443.

Gottlieb, E. W., Wright, E. L., and Liller, W. 1975. Optical studies of Uhuru sources. XI. A probable period for Scorpius X-1 = V818 Scorpii. *ApJL*, **195**, L33–L35.

Grindlay, J. E., McClintock, J. E., Canizares, C. R., Cominsky, L., Li, F. K., Lewin, W. H. G., and van Paradijs, J. 1978. Discovery of optical bursts from an X-ray burst source, MXB 1735–44. *Nature*, **274**, 567–568.

Hackwell, J. A., Grasdalen, G. L., Gehrz, R. D., Cominsky, L., Lewin, W. H. G., and van Paradijs, J. 1979. The detection of an optical burst coincident with an X-ray burst from MXB 1837+05 (Ser X-1). *ApJL*, **233**, L115–L119.

Hameury, J.-M., Lasota, J.-P., and Warner, B. 2000. The zoo of dwarf novae: illumination, evaporation and disc radius variation. *A&A*, **353**, 244–252.

Haswell, C. A., Robinson, E. L., Horne, K., Stiening, R. F., and Abbott, T. M. C. 1993. On the mass of the compact object in the black hole binary A0620-00. *ApJ*, **411**, 802–812.

Haswell, C. A., King, A. R., Murray, J. R., and Charles, P. A. 2001. Superhumps in low-mass X-ray binaries. *MNRAS*, **321**, 475–480.

Haswell, C. A., Hynes, R. I., King, A. R., and Schenker, K. 2002. The ultraviolet line spectrum of the soft X-ray transient XTE J1118+480: a CNO-processed core exposed. *MNRAS*, **332**, 928–932.

Hellier, C. 2001. On Echo Outbursts and ER UMa Supercycles in SU UMa-Type Cataclysmic Variables. *PASP*, **113**, 469–472.

Horne, K. 1994. Echo Mapping Problems Maximum Entropy solutions. Pages 23–25 of: P. M. Gondhalekar, K. Horne, & B. M. Peterson (ed), *Reverberation Mapping of the Broad-Line Region in Active Galactic Nuclei*. Astronomical Society of the Pacific Conference Series, vol. 69.

Horne, K., and Marsh, T. R. 1986. Emission line formation in accretion discs. *MNRAS*, **218**, 761–773.

Hynes, R. I. 2005. The Optical and Ultraviolet Spectral Energy Distributions of Short-Period Black Hole X-Ray Transients in Outburst. *ApJ*, **623**, 1026–1043.

Hynes, R. I., and Haswell, C. A. 1999. Hubble Space Telescope observations of the black hole X-ray transient GRO J0422+32 near quiescence. *MNRAS*, **303**, 101–106.

Hynes, R. I., O'Brien, K., Horne, K., Chen, W., and Haswell, C. A. 1998. Echoes from an irradiated disc in GRO J1655-40. *MNRAS*, **299**, L37–L41.

Hynes, R. I., Mauche, C. W., Haswell, C. A., Shrader, C. R., Cui, W., and Chaty, S. 2000. The X-Ray Transient XTE J1118+480: Multiwavelength Observations of a Low-State Minioutburst. *ApJL*, **539**, L37–L40.

Hynes, R. I., Charles, P. A., Haswell, C. A., Casares, J., Zurita, C., and Serra-Ricart, M. 2001. Optical studies of the X-ray transient XTE J2123-058 - II. Phase-resolved spectroscopy. *MNRAS*, **324**, 180–190.

Hynes, R. I., Haswell, C. A., Chaty, S., Shrader, C. R., and Cui, W. 2002. The evolving accretion disc in the black hole X-ray transient XTE J1859+226. *MNRAS*, **331**, 169–179.

Hynes, R. I., Steeghs, D., Casares, J., Charles, P. A., and O'Brien, K. 2003a. Dynamical Evidence for a Black Hole in GX 339-4. *ApJL*, **583**, L95–L98.

Hynes, R. I., Charles, P. A., Casares, J., Haswell, C. A., Zurita, C., and Shahbaz, T. 2003b. Fast photometry of quiescent soft X-ray transients with the Acquisition Camera on Gemini-South. *MNRAS*, **340**, 447–456.

Hynes, R. I., Haswell, C. A., Cui, W., Shrader, C. R., O'Brien, K., Chaty, S., Skillman, D. R., Patterson, J., and Horne, K. 2003c. The remarkable rapid X-ray, ultraviolet, optical and infrared variability in the black hole XTE J1118+480. *MNRAS*, **345**, 292–310.

Hynes, R. I., Robinson, E. L., and Bitner, M. 2005. Observational Constraints on Cool Disk Material in Quiescent Black Hole Binaries. *ApJ*, **630**, 405–412.

Hynes, R. I., Robinson, E. L., Pearson, K. J., Gelino, D. M., Cui, W., Xue, Y. Q., Wood, M. A., Watson, T. K., Winget, D. E., and Silver, I. M. 2006a. Further Evidence for Variable Synchrotron Emission in XTE J1118+480 in Outburst. *ApJ*, **651**, 401–407.

Hynes, R. I., Horne, K., O'Brien, K., Haswell, C. A., Robinson, E. L., King, A. R., Charles, P. A., and Pearson, K. J. 2006b. Multiwavelength Observations of EXO 0748-676. I. Reprocessing of X-Ray Bursts. *ApJ*, **648**, 1156–1168.

Hynes, R. I., Brien, K. O., Mullally, F., and Ashcraft, T. 2009a. Echo mapping of Swift J1753.5-0127. *MNRAS*, **399**, 281–286.

Hynes, R. I., Bradley, C. K., Rupen, M., Gallo, E., Fender, R. P., Casares, J., and Zurita, C. 2009b. The quiescent spectral energy distribution of V404 Cyg. *MNRAS*, **399**, 2239–2248.

Ilovaisky, S. A., Chevalier, C., White, N. E., Mason, K. O., Sanford, P. W., Delvaille, J. P., and Schnopper, H. W. 1980. Simultaneous X-ray and optical observations of rapid variability in Scorpius X-1. *MNRAS*, **191**, 81–93.

Johnston, H. M., Kulkarni, S. R., and Oke, J. B. 1989. The black hole A0620-00 and its accretion disk. *ApJ*, **345**, 492–497.

Jonker, P. G., Steeghs, D., Nelemans, G., and van der Klis, M. 2005. The radial velocity of the companion star in the low-mass X-ray binary 2S 0921-630: limits on the mass of the compact object. *MNRAS*, **356**, 621–626.

Kanbach, G., Straubmeier, C., Spruit, H. C., and Belloni, T. 2001. Correlated fast X-ray and optical variability in the black-hole candidate XTE J1118+480. *Nature*, **414**, 180–182.

King, A. R., and Ritter, H. 1998. The light curves of soft X-ray transients. *MNRAS*, **293**, L42–L48.

Koen, C. 2003. The analysis of indexed astronomical time-series - VIII. Cross-correlating noisy autoregressive series. *MNRAS*, **344**, 798–808.

Kong, A. K. H., McClintock, J. E., Garcia, M. R., Murray, S. S., and Barret, D. 2002. The X-Ray Spectra of Black Hole X-Ray Novae in Quiescence as Measured by Chandra. *ApJ*, **570**, 277–286.

Kuulkers, E. 1998. A0620-00 revisited: a black-hole transient case-study. *New Astronomy Review*, **42**, 1–22.

Lasota, J.-P. 2001. The disc instability model of dwarf novae and low-mass X-ray binary transients. *New Astronomy Review*, **45**, 449–508.

Lawrence, A., Cominsky, L., Engelke, C., Jernigan, G., Lewin, W. H. G., Matsuoka, M., Mitsuda, K., Oda, M., Ohashi, T., Pedersen, H., and van Paradijs, J. 1983. Simultaneous U, B, V, and X-ray measurements of a burst from 4U/MXB 1636-53. *ApJ*, **271**, 793–803.

Lewin, W. H. G., and van der Klis, M. (eds). 2006. *Compact stellar X-ray sources*. Cambridge Astrophysics Series, vol. 39. Cambridge University Press.

Lewin, W. H. G., van Paradijs, J., and van den Heuvel, E. P. J. (eds). 1995. *X-ray binaries*. Cambridge Astrophysics Series, vol. 26. Cambridge University Press.

Lynden-Bell, D. 1969. Galactic Nuclei as Collapsed Old Quasars. *Nature*, **223**, 690–694.

Markoff, S., Falcke, H., and Fender, R. 2001. A jet model for the broadband spectrum of XTE J1118+480. Synchrotron emission from radio to X-rays in the Low/Hard spectral state. *A&A*, **372**, L25–L28.

Marsh, T. R. 2001. Doppler Tomography. Pages 1–26 of: H. M. J. Boffin, D. Steeghs, & J. Cuypers (ed), *Astrotomography, Indirect Imaging Methods in Observational Astronomy*. Lecture Notes in Physics, Berlin Springer Verlag, vol. 573.

Marsh, T. R., Robinson, E. L., and Wood, J. H. 1994. Spectroscopy of A0620-00 - the Mass of the Black-Hole and an Image of its Accretion Disc. *MNRAS*, **266**, 137–154.

Mason, K. O., Seitzer, P., Tuohy, I. R., Hunt, L. K., Middleditch, J., Nelson, J. E., and White, N. E. 1980. A 5.57 hr modulation in the optical counterpart of 2S 1822–371. *ApJL*, **242**, L109–L113.

McClintock, J. E., and Remillard, R. A. 1986. The black hole binary A0620-00. *ApJ*, **308**, 110–122.

McClintock, J. E., and Remillard, R. A. 2000. HST/STIS UV Spectroscopy of Two Quiescent X-Ray Novae: A0620-00 and Centaurus X-4. *ApJ*, **531**, 956–962.

McClintock, J. E., Canizares, C. R., and Tarter, C. B. 1975. On the origin of 4640-4650 A emission in X-ray stars. *ApJ*, **198**, 641–652.

McClintock, J. E., Canizares, C. R., Cominsky, L., Li, F. K., Lewin, W. H. G., van Paradijs, J., and Grindlay, J. E. 1979. A 3-s delay in an optical burst from X-ray burst source MXB 1735–44. *Nature*, **279**, 47–49.

McClintock, J. E., Horne, K., and Remillard, R. A. 1995. The dim inner accretion disk of the quiescent black hole A0620-00. *ApJ*, **442**, 358–365.

McClintock, J. E., Narayan, R., Garcia, M. R., Orosz, J. A., Remillard, R. A., and Murray, S. S. 2003. Multiwavelength Spectrum of the Black Hole XTE J1118+480 in Quiescence. *ApJ*, **593**, 435–451.

McGowan, K. E., Charles, P. A., O'Donoghue, D., and Smale, A. P. 2003. Correlated optical and X-ray variability in LMC X-2. *MNRAS*, **345**, 1039–1048.

Migliari, S., Tomsick, J. A., Maccarone, T. J., Gallo, E., Fender, R. P., Nelemans, G., and Russell, D. M. 2006. Spitzer Reveals Infrared Optically Thin Synchrotron Emission from the Compact Jet of the Neutron Star X-Ray Binary 4U 0614+091. *ApJL*, **643**, L41–L44.

Migliari, S., Tomsick, J. A., Miller-Jones, J. C. A., Heinz, S., Hynes, R. I., Fender, R. P., Gallo, E., Jonker, P. G., and Maccarone, T. J. 2009. The complete spectrum of the neutron star X-ray binary 4U0614+091. *ApJ*, **710**, 117–124.

Mirabel, I. F., and Rodríguez, L. F. 1994. A superluminal source in the Galaxy. *Nature*, **371**, 46–48.

Motch, C., Ilovaisky, S. A., and Chevalier, C. 1982. Discovery of fast optical activity in the X-ray source GX 339-4. *A&A*, **109**, L1–L4.

Motch, C., Ricketts, M. J., Page, C. G., Ilovaisky, S. A., and Chevalier, C. 1983. Simultaneous X-ray/optical observations of GX339-4 during the May 1981 optically bright state. *A&A*, **119**, 171–176.

Muñoz-Darias, T., Casares, J., and Martínez-Pais, I. G. 2005. The "K-Correction" for Irradiated Emission Lines in LMXBs: Evidence for a Massive Neutron Star in X1822-371 (V691 CrA). *ApJ*, **635**, 502–507.

Muñoz-Darias, T., Martínez-Pais, I. G., Casares, J., Dhillon, V. S., Marsh, T. R., Cornelisse, R., Steeghs, D., and Charles, P. A. 2007. Echoes from the companion star in Sco X-1. *MNRAS*, **379**, 1637–1646.

Muno, M. P., and Mauerhan, J. 2006. Mid-Infrared Emission from Dust around Quiescent Low-Mass X-Ray Binaries. *ApJL*, **648**, L135–L138.

Narayan, R., and McClintock, J. E. 2005. Inclination Effects and Beaming in Black Hole X-Ray Binaries. *ApJ*, **623**, 1017–1025.

Narayan, R., and Raymond, J. 1999. Thermal X-Ray Line Emission from Accreting Black Holes. *ApJL*, **515**, L69–L72.

Narayan, R., McClintock, J. E., and Yi, I. 1996. A New Model for Black Hole Soft X-Ray Transients in Quiescence. *ApJ*, **457**, 821–833.

Narayan, R., Barret, D., and McClintock, J. E. 1997. Advection-dominated Accretion Model of the Black Hole V404 Cygni in Quiescence. *ApJ*, **482**, 448–464.

Neil, E. T., Bailyn, C. D., and Cobb, B. E. 2007. Infrared Monitoring of the Microquasar GRS 1915+105: Detection of Orbital and Superhump Signatures. *ApJ*, **657**, 409–414.

Nelemans, G., Jonker, P. G., Marsh, T. R., and van der Klis, M. 2004. Optical spectra of the carbon-oxygen accretion discs in the ultra-compact X-ray binaries 4U 0614+09, 4U 1543-624 and 2S 0918-549. *MNRAS*, **348**, L7–L11.

Nelemans, G., Jonker, P. G., and Steeghs, D. 2006. Optical spectroscopy of (candidate) ultracompact X-ray binaries: constraints on the composition of the donor stars. *MNRAS*, **370**, 255–262.

O'Brien, K., Horne, K., Hynes, R. I., Chen, W., Haswell, C. A., and Still, M. D. 2002. Echoes in X-ray binaries. *MNRAS*, **334**, 426–434.

O'Donoghue, D., and Charles, P. A. 1996. Have superhumps been seen in black hole soft X-ray transients? *MNRAS*, **282**, 191–205.

Ogilvie, G. I., and Dubus, G. 2001. Precessing warped accretion discs in X-ray binaries. *MNRAS*, **320**, 485–503.

Orosz, J. A. 2001. The spectroscopic mass ratio of the black hole binary XTE J1118+480. *The Astronomer's Telegram*, **67**.

Orosz, J. A., and Kuulkers, E. 1999. The optical light curves of Cygnus X-2 (V1341 Cyg) and the mass of its neutron star. *MNRAS*, **305**, 132–142.

Orosz, J. A., McClintock, J. E., Narayan, R., Bailyn, C. D., Hartman, J. D., Macri, L., Liu, J., Pietsch, W., Remillard, R. A., Shporer, A., and Mazeh, T. 2007. A 15.65-solar-mass black hole in an eclipsing binary in the nearby spiral galaxy M 33. *Nature*, **449**, 872–875.

Osaki, Y., Meyer, F., and Meyer-Hofmeister, E. 2001. Repetitive rebrightening of EG Cancri: Evidence for viscosity decay in the quiescent disk? *A&A*, **370**, 488–495.

Özel, F., and Psaltis, D. 2009. Reconstructing the neutron-star equation of state from astrophysical measurements. *Phys. Rev. D*, **80**, 103003.

Parmar, A. N., White, N. E., Giommi, P., Haberl, F., Pedersen, H., and Mayor, M. 1985. EXO 0748-676. *IAU Circ.*, **4039**.

Patterson, J., Kemp, J., Skillman, D. R., Harvey, D. A., Shafter, A. W., Vanmunster, T., Jensen, L., Fried, R., Kiyota, S., Thorstensen, J. R., and Taylor, C. J. 1998. Superhumps in Cataclysmic Binaries. XV. EG Cancri, King of the Echo Outbursts. *PASP*, **110**, 1290–1303.

Pearson, K. J., Hynes, R. I., Steeghs, D., Jonker, P. G., Haswell, C. A., King, A. R., O'Brien, K., Nelemans, G., and Méndez, M. 2006. Multiwavelength Observations of EXO 0748-676. II. Emission-Line Behavior. *ApJ*, **648**, 1169–1180.

Pedersen, H., Lub, J., Inoue, H., Koyama, K., Makishima, K., Matsuoka, M., Mitsuda, K., Murakami, T., Oda, M., Ogawara, Y., Ohashi, T., Shibazaki, N., Tanaka, Y., Hayakawa, S., Kunieda, H., Makino, F., Masai, K., Nagase, F., Tawara, Y., Miyamoto, S., Tsunemi, H., Yamashita, K., Kondo, I., Jernigan, J. G., van Paradijs, J., Beardsley, A., Cominsky, L., Doty, J., and Lewin, W. H. G. 1982. Simultaneous optical and X-ray bursts from 4U/MXB 1636-53. *ApJ*, **263**, 325–339.

Peterson, B. M., and Horne, K. 2006. Reverberation mapping of active galactic nuclei. Page 89 of: M. Livio & S. Casertano (ed), *Planets to Cosmology: Essential Science in the Final Years of the Hubble Space Telescope*.

Petro, L. D., Bradt, H. V., Kelley, R. L., Horne, K., and Gomer, R. 1981. Rapid X-ray and optical flares from Scorpius X-1. *ApJL*, **251**, L7–L11.

Pfahl, E., Rappaport, S., and Podsiadlowski, P. 2003. The Galactic Population of Low- and Intermediate-Mass X-Ray Binaries. *ApJ*, **597**, 1036–1048.

Pietsch, W., Steinle, H., and Gottwald, M. 1983. 4U 2129+47 = V1727 Cygni. *IAU Circ.*, **3887**.

Quataert, E., and Narayan, R. 1999. Spectral Models of Advection-dominated Accretion Flows with Winds. *ApJ*, **520**, 298–315.

Reynolds, M. T., Callanan, P. J., and Filippenko, A. V. 2007. Keck infrared observations of GRO J0422+32 in quiescence. *MNRAS*, **374**, 657–663.

Sandage, A., Osmer, P., Giacconi, R., Gorenstein, P., Gursky, H., Waters, J., Bradt, H., Garmire, G., Sreekantan, B. V., Oda, M., Osawa, K., and Jugaku, J. 1966. On the optical identification of Sco X-1. *ApJ*, **146**, 316–321.

Shahbaz, T., Ringwald, F. A., Bunn, J. C., Naylor, T., Charles, P. A., and Casares, J. 1994. The mass of the black hole in V404 Cygni. *MNRAS*, **271**, L10–L14.

Shahbaz, T., Bandyopadhyay, R., Charles, P. A., and Naylor, T. 1996. Infrared spectroscopy of V404 Cygni: limits on the accretion disc contamination. *MNRAS*, **282**, 977–981.

Shahbaz, T., Dhillon, V. S., Marsh, T. R., Zurita, C., Haswell, C. A., Charles, P. A., Hynes, R. I., and Casares, J. 2003. Multicolour observations of V404 Cyg with ULTRACAM. *MNRAS*, **346**, 1116–1124.

Shahbaz, T., Casares, J., Watson, C. A., Charles, P. A., Hynes, R. I., Shih, S. C., and Steeghs, D. 2004. The Massive Neutron Star or Low-Mass Black Hole in 2S 0921-630. *ApJL*, **616**, L123–L126.

Shahbaz, T., Dhillon, V. S., Marsh, T. R., Casares, J., Zurita, C., Charles, P. A., Haswell, C. A., and Hynes, R. I. 2005. ULTRACAM observations of the black hole X-ray transient XTE J1118+480 in quiescence. *MNRAS*, **362**, 975–982.

Shahbaz, T., Fender, R. P., Watson, C. A., and O'Brien, K. 2008a. The First Polarimetric Signatures of Infrared Jets in X-Ray Binaries. *ApJ*, **672**, 510–515.

Shahbaz, T., Watson, C. A., Zurita, C., Villaver, E., and Hernandez-Peralta, H. 2008b. Time-Resolved Optical Photometry of the Ultracompact Binary 4U 0614+091. *PASP*, **120**, 848–851.

Shakura, N. I., and Sunyaev, R. A. 1973. Black holes in binary systems. Observational appearance. *A&A*, **24**, 337–355.

Smith, A. J., Haswell, C. A., Murray, J. R., Truss, M. R., and Foulkes, S. B. 2007. Comprehensive simulations of superhumps. *MNRAS*, **378**, 785–800.

Steeghs, D. 2003. Extending emission-line Doppler tomography: mapping-modulated line flux. *MNRAS*, **344**, 448–454.

Steeghs, D., and Casares, J. 2002. The Mass Donor of Scorpius X-1 Revealed. *ApJ*, **568**, 273–278.

Strohmayer, T., and Bildsten, L. 2006. New views of thermonuclear bursts. Pages 113–156 of: Lewin, W. H. G. & van der Klis, M. (ed), *Compact stellar X-ray sources*. Cambridge University Press.

Thorstensen, J., Charles, P., Bowyer, S., Briel, U. G., Doxsey, R. E., Griffiths, R. E., and Schwartz, D. A. 1979. A precise position and optical identification for 4U 2129+47 - X-ray heating and a 5.2 hour binary period. *ApJL*, **233**, L57–L61.

Truss, M. R., Wynn, G. A., Murray, J. R., and King, A. R. 2002. The origin of the rebrightening in soft X-ray transient outbursts. *MNRAS*, **337**, 1329–1339.

Uemura, M., Kato, T., Matsumoto, K., Honkawa, M., Cook, L., Martin, B., Masi, G., Oksanen, A., Moilanen, M., Novak, R., Sano, Y., and Ueda, Y. 2000. XTE J1118+480. *IAU Circ.*, **7418**.

van der Klis, M. 2006. Rapid X-ray Variability. Pages 39–112 of: Lewin, W. H. G. & van der Klis, M. (ed), *Compact stellar X-ray sources*. Cambridge Astrophysics Series, vol. 39. Cambridge University Press.

von Zeipel, H. 1924. The radiative equilibrium of a rotating system of gaseous masses. *MNRAS*, **84**, 665–683.

Wade, R. A., and Horne, K. 1988. The radial velocity curve and peculiar TiO distribution of the red secondary star in Z Chamaeleontis. *ApJ*, **324**, 411–430.

White, N. E., and Swank, J. H. 1982. The discovery of 50 minute periodic absorption events from 4U 1915-05. *ApJL*, **253**, L61–L66.

Whitehurst, R., and King, A. 1991. Superhumps, resonances and accretion discs. *MNRAS*, **249**, 25–35.

Wijers, R. A. M. J., and Pringle, J. E. 1999. Warped accretion discs and the long periods in X-ray binaries. *MNRAS*, **308**, 207–220.

Wolff, M. T., Ray, P. S., Wood, K. S., and Hertz, P. L. 2009. Eclipse Timings of the Transient Low-Mass X-ray Binary EXO 0748-676. IV. The Rossi X-ray Timing Explorer Eclipses. *ApJS*, **183**, 156–170.

Zurita, C., Casares, J., Shahbaz, T., Charles, P. A., Hynes, R. I., Shugarov, S., Goransky, V., Pavlenko, E. P., and Kuznetsova, Y. 2000. Optical studies of the X-ray transient XTE J2123-058 - I. Photometry. *MNRAS*, **316**, 137–142.

Zurita, C., Casares, J., Shahbaz, T., Wagner, R. M., Foltz, C. B., Rodríguez-Gil, P., Hynes, R. I., Charles, P. A., Ryan, E., Schwarz, G., and Starrfield, S. G. 2002. Detection of superhumps in XTE J1118+480 approaching quiescence. *MNRAS*, **333**, 791–799.